Source-explicit estimation of brown carbon in the polluted atmosphere over North China Plain: implications for distribution, absorption and direct radiative effect

Jiamao Zhou[1,2], Jiarui Wu[1], Xiaoli Su[1], Ruonan Wang[1], Imad EI Haddad[4], Xia Li[1], Qian Jiang[1], Ting Zhang[1], Wenting Dai[1], Junji Cao[3], Andre S.H. Prevot[4], Xuexi Tie[1], Guohui Li[1]

[1]Key Laboratory of Aerosol Chemistry and Physics, State Key Laboratory of Loess and Quaternary Geology, Institute of Earth Environment, Chinese Academy of Sciences, Xi'an 710061, China

[2]Guanzhong Plain Ecological Environment Change and Comprehensive Treatment National Observation and Research Station, Xi'an 710061, China

[3]Institute of Atmospheric Physics, Chinese Academy of Sciences, Beijing 100029, China

[4]PSI Center for Energy and Environmental Sciences, Paul Scherrer Institute, 5232 Villigen, Switzerland

Correspondence to: Guohui Li (ligh@ieecas.cn)

设置了格式: 上标, 突出显示

设置了格式: 上标, 突出显示

带格式的: 两端对齐

设置了格式: 上标

设置了格式: 字体: (中文) +中文正文 (等线), (中文) 中文 (中国)

Abstract. Brown carbon (BrC) plays a significant role in altering atmospheric radiation. Beyond biomass and biofuel combustion, recent studies identify fossil fuel sources—especially residential coal burning and vehicle exhaust—as major contributors to BrC. This underscores a gap in climate models, which often assume fossil fuel organic aerosols (OA) are non-absorbing or treat all OA as light-scattering. In this study, we simulate BrC over the North China Plain (NCP) during a winter pollution event using the WRF-Chem model, incorporating explicit BrC absorption properties. The model aligns well with observed pollutant and aerosol levels, revealing an average near-surface BrC concentration of 5.24.8 μg m^{-3}, contributing 14.26.4% to aerosol absorption at 365 nm. Using a diagnostic adjoint approach, we estimate that BrC exerts a direct radiative effect (DRE) averaging -0.0910 W m^{-2} at the top of the atmosphere, reducing the cooling effect of organic carbon by 28.04% and producing a local warming effect of up to +0.4034 W m^{-2}. Coal combustion is the largest BrC source in the NCP in 2014, though secondary BrC also significantly impacts the regional radiation balance.

Key words: Brown Carbon, emission sources, absorption, direct radiative effect

设置了格式: 突出显示

设置了格式: 突出显示

设置了格式: 突出显示

1 Introduction

Brown Carbon (BrC) is a collective component for those colored organic compounds with wavelength dependent light-absorption properties (Mukai and Ambe, 1986; Kirchstetter et al., 2004; Andreae and Gelencsér, 2006). BrC has been recognized as an important short-lived climate forcer contributing considerably to climate change by warming of the atmosphere (IPCC, 2013; Feng et al., 2013; Jacobson, 2014; Jo et al., 2016; Brown et al., 2018). A study suggested that the light absorption induced by BrC can be equal to or even higher than that of black carbon (Pokhrel et al., 2017), and substantially influences atmospheric radiative forcing. Recent studies have shown that BrC accounts for 30%~50% of the total absorption of aerosols in Atlanta USA, Brazil and Hebei China (Hoffer et al., 2006; Yang et al., 2009; Liu et al., 2013). The direct radiation effect (DRE) caused by BrC is greater than +1 W m^{-2} in some regions, such as South Asia, Africa and Southeast Asia, much higher than the global average (Park et al., 2010; Feng et al., 2013; Lin et al., 2014; Saleh et al., 2014; Jo et al., 2016; Wang et al., 2018; Yan et al., 2018). ~~As a result, BrC reduces the cooling effect caused by organic aerosols by approximately 16% .~~ However, the modelled ~~evaluated~~ DRE associated with BrC ~~is~~ remains highly uncertain, with variations spanning an order of magnitude difference. ~~, e.g.~~In particular, the estimated global DRE of BrC is in the range between +0.03 W/m^2 to +0.57 W/m^2 (Hammer et al., 2016), which is caused by the limited observations of BrC mass and absorption properties ~~observations~~ (Tuccella et al., 2020; Saleh, 2020).

It has been well established that BrC is not a single substance, but a general term for light-absorbing organic aerosols. ~~Currently, the sources and chemical composition of BrC is not completely understood yet.~~ A series of laboratory measurements and observations in the earlier years demonstrate that BrC is mainly associated with smoldering biomass burning (BB) or biofuel (BFs) combustion (Chakrabarty et al., 2010; Chen and Bond, 2010; Lack et al., 2012; Washenfelder et al., 2015; Kumar et al., 2018). On the other hand, OA from fossil-fuel combustion are generally assumed to be non-absorbing as the combustion conditions for fossil fuels (FFs) are typically not conducive for BrC formation (Hecobian et al., 2010; Shapiro et al., 2009; Bond et al., 2013). Therefore, earlier climate model studies have assumed that primary OA from BB and BFs combustion is the main or sole BrC source (Feng et al., 2013; Jacobson, 2014; Saleh et al., 2014; Hammer et al., 2016; Brown et al., 2018). Recent studies have also incorporated the ageing of secondary organic aerosol (SOA) (Jo et al., 2016; Wang et al., 2018; Zhang et al., 2020). However, more recent exceptions are being found in low-efficiency residential-coal combustion (RCC) (Bond, 2001; Yan et al., 2017; Xie et al., 2019; Tian et al., 2019; Zhang et al., 2022a) and fuel-oil combustion in vehicle and ship engines (Xie et al., 2017; Corbin et al., 2019; Tang et al., 2020; Huang et al.,

设置了格式: 突出显示
设置了格式: 突出显示
设置了格式: 突出显示
设置了格式: 突出显示
设置了格式: 突出显示
设置了格式: 突出显示
设置了格式: 突出显示
设置了格式: 突出显示
设置了格式: 突出显示
设置了格式: 突出显示
设置了格式: 突出显示
设置了格式: 字体: (默认) Times New Roman, 10 磅, 突出显示
设置了格式: 字体: (默认) Times New Roman, 10 磅, 突出显示
设置了格式: 突出显示
设置了格式: 突出显示
设置了格式: 突出显示
设置了格式: 突出显示
设置了格式: 突出显示
设置了格式: 突出显示
设置了格式: 突出显示

2022). It is now generally accepted that the formation of BrC is not exclusively linked to the chemical make-up of biomass fuels but is most critically determined by the combustion conditions (Saleh et al., 2018; Cheng et al., 2020; Saleh, 2020; Wang et al., 2022a). The key factor contributing to the high levels of BrC observed from biomass fuels is their combustion under relatively low-temperature and fuel-rich conditions, which are highly favorable for BrC formation. In contrast, fossil fuels, such as those burned in internal combustion engines, typically undergo combustion at higher temperatures and under more fuel-lean conditions, which are less conducive to BrC production (Saleh, 2020). China, as a developing country, coal is commonly used for residential heating in cold season, causing massive emissions of organic particles (Yan et al., 2017; Li et al., 2018). According to the National Bureau of Statistics of China (https://data.stats.gov.cn), the coal consumption in 2014 was about 4000 Tg, accounting for 65.8% of the total primary energy use of China. Of this, around 93 Tg is used as household fuel. The poor burning conditions and limited emission control facilities in this region could lead to substantial emissions of BrC. This could explain why, to date, all reported instances of coal-derived BrC have originated from China. Both Yan et a., (2017) and Mo et al., (2021) have used dual carbon isotope-based source apportionment method reported that fossil fuel, especially coal combustion from the residential sector is important source in northern China, even the largest contributor in some regions.

These recent findings indicate a critical gap on the treatment of BrC ~~in~~in chemical transport models, atmospheric chemistry models and climate models as well ~~climate models~~, which present an even greater concern, as they typically do not consider BrC at all (Ma et al., 2021; Jo et al., 2023; Gao et al., 2025; Ge et al., 2025). ~~This includes~~Addressing this gap requires expanding the scope of BrC sources, ~~and~~ assigning distinct optical properties for each source and incorporating those that have been underrepresented or overlooked in past assessments into numerical models. In this study, we include the main primary emission sources (RCC, BB, BFs, ~~vehicle emissions~~FFs-TRA) of BrC and secondary derived BrC in a regional model, the Weather Research and Forecasting model coupled with Chemistry (WRF-Chem). A representative region, North China Plain (NCP), is chosen as the study domain with high anthropogenic carbonaceous aerosols due to the widespread use of coal and biomass burning for heating during winter and the increasing number of motor vehicles. We performed a month simulation to evaluate the surface distribution, absorption and the DRE of BrC in the NCP, by updating BrC optical properties of different sources. Sensitivity experiments have also been devised to assess the contribution of BrC from major sources.

设置了格式: 突出显示

2 Model and Method

2.1 WRF-Chem Model and configurations

The WRF-Chem model (Grell et al., 2005; Fast et al., 2006) modified by Li et al., (2010; 2011a; 2011b; 2012) is used to quantitatively estimate the BrC in the NCP. A heavily polluted month from January 1 to 30, 2014 is selected for the simulation period. The anthropogenic emissions are developed by Zhang et al. (2009) and Li et al. (2017), including five sources ~~contributed from~~ , namely agriculture, industry, power generation, residential, and transportation ~~sources~~. The biogenic emissions are calculated online using the MEGAN (Model of Emissions of Gases and Aerosol from Nature) model developed by Guenther et al. (2006). Additionally, the grid-based RCC, BB and BFs combustion emissions are used to update the BrC sources in this study ~~which will be~~, described later. The model simulation domain is shown in Fig. 1. The detailed model description and configurations can be found in supplementary text S1 ~~.1~~ and Table S1, respectively.

设置了格式: 突出显示

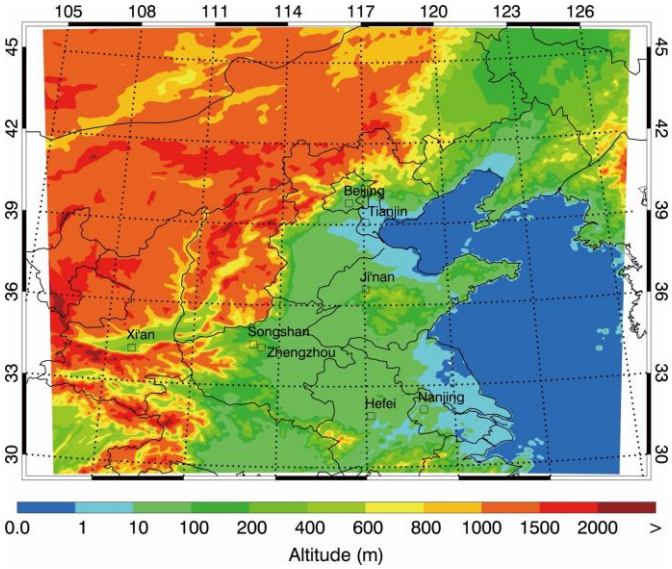

Figure 1. WRF-Chem simulation domain with topography. The square denotes the field sites for simulation and observation comparison

2.2 Aerosol radiative module

The aerosol radiative module developed by Li et al., (2011a) has been incorporated into the WRF-Chem model to calculate the aerosol optical depth (AOD or τ_a), single scattering albedo (SSA or ω_a), and the asymmetry factor (g_a). In the aerosol module, aerosols are represented by a three-moment approach with a

lognormal size distribution:

$$n(lnD) = \frac{N}{\sqrt{2\pi}ln\sigma_g} exp[-\frac{1}{2}(\frac{lnD-lnD_g}{ln\sigma_g})^2] \quad (1)$$

Where D is the particle diameter, N is the number distribution of all particles in the distribution, D_g is the geometric mean diameter, and σ_g is the geometric standard deviation. To calculate the aerosol optical properties, the aerosol spectrum is divided into 48 bins from 0.002 to 20.0 μm, with radius r_i. The aerosols are classified into four types: (1) internally mixed sulfate, nitrate, ammonium, hydrophilic organics and black carbon (BC), and water; (2) hydrophobic organics; (3) hydrophobic BC; and (4) other unidentified aerosols (generally dust-like aerosols). These four kinds of aerosols are assumed to be mixed externally. For the internally mixed aerosols, the complex refractive index at a specific wavelength (λ) is calculated based on the volume-weighted average of the individual refractive index. Given the particle size and complex refractive index, the extinction efficiency (Q_e), ω_a and g_a are calculated using the Mie theory at a certain wavelength (λ). The look-up tables of Q_e, ω_a and g_a are established according to particle sizes and refractive indices to avoid multiple Mie scattering calculation. The aerosol optical parameters are interpolated linearly from the look-up tables with the calculated refractive index and particle size in the module. The τ_a at a certain λ in a given atmospheric layer k is determined by the summation over all types of aerosols and all bins:

$$\tau_a(\lambda,k) = \sum_{i=1}^{48}\sum_{j}^{4} Q_e(\lambda,r_i,j,k)\pi r_i^2 n(r_i,j,k)\Delta Z_k \quad (2)$$

where $n(r_i,j,k)$ is the number concentration of j-th kind of aerosols in the i-th bin. ΔZ_k is the depth of an atmospheric layer. The weighted-mean values of ω_a and g_a are then calculated by using D'Almeida et al., (1991):

$$\omega_a(\lambda,k) = \frac{\sum_{i=1}^{48}\sum_{j}^{4} Q_e(\lambda,r_i,j,k)\pi r_i^2 n(r_i,j,k)\omega_a(\lambda,r_i,j,k)\Delta Z_k}{\sum_{i=1}^{48}\sum_{j}^{4} Q_e(\lambda,r_i,j,k)\pi r_i^2 n(r_i,j,k)\Delta Z_k} \quad (3)$$

$$g_a(\lambda,k) = \frac{\sum_{i=1}^{48}\sum_{j}^{4} Q_e(\lambda,r_i,j,k)\pi r_i^2 n(r_i,j,k)\omega_a(\lambda,r_i,j,k)g_a(\lambda,r_i,j,k)\Delta Z_k}{\sum_{i=1}^{48}\sum_{j}^{4} Q_e(\lambda,r_i,j,k)\pi r_i^2 n(r_i,j,k)\omega_a(r_i,j,k)\Delta Z_k} \quad (4)$$

When the wavelength-dependent τ_a, ω_a, and g_a are calculated, they can be used in the Goddard shortwave module.

It is worth noting that the aerosol liquid water content in the study is predicted with the inorganic aerosols using a computationally efficient thermodynamic equilibrium model, ISORROPIA (version 1.7, (Nenes et al., 1998; Fountoukis and Nenes, 2007). In this study, ISORROPIA is mainly used to predict the thermodynamic equilibrium between the ammonium-sulfate-nitrate-chloride-water aerosols and their gas-phase precursors H_2SO_4-HNO_3-NH_3-HCL-water vapor, and water uptake of aerosols is calculated using the Zdanovskii-

设置了格式: 突出显示
设置了格式: 突出显示
设置了格式: 突出显示
设置了格式: 突出显示
设置了格式: 突出显示
带格式的: 缩进: 首行缩进: 0 字符, 制表位: 不在 2 字符
带格式的: 首行缩进: 0 字符, 制表位: 不在 2 字符
设置了格式: 突出显示
设置了格式: 突出显示
设置了格式: 下标, 突出显示
设置了格式: 突出显示
设置了格式: 下标, 突出显示
设置了格式: 突出显示
设置了格式: 下标, 突出显示
设置了格式: 突出显示
设置了格式: 下标, 突出显示
设置了格式: 突出显示
设置了格式: 突出显示
设置了格式: 突出显示

Stokes-Robinson (ZSR) correlation (Stokes and Robinson, 1966):

$$W = \sum_i \frac{M_i}{m_{oi}(a_w)} \quad (5)$$

Where W is the mass concentration of aerosol liquid water (kg m^{-3} air), M_i is the molar concentration of species i (mol m^{-3} air), and $m_{oi}(a_w)$ is the molality of an aqueous binary solution of the i-th electrolyte with the same a_w (i.e. relative humidity) as in the multicomponent solution.

The BrC in the model has an effective density of 1.2 g cm^{-3} for primary BrC (Turpin and Lim, 2001) and of 1.00 g cm^{-3} for secondary BrC~~.~~ (Hurley et al., 2001)~~.~~ The imaginary refractive index of BrC used in this study is discussed in 2.3.2.

2.3 Model modifications

2.3.1 Source separation of BrC

The definition of BrC in the model is dependent on its sources. Due to the lack of BrC emission inventories, ~~most of the previous studies either simply use OA from BB as a proxy of BrC or estimate the emission of BrC based on the emission ratio of BrC versus BC (Zhu et al., 2021).~~ According to the characteristics of energy structure in China, assumptions and code modifications of the WRF-Chem model have been made to consider the ~~primary~~ BrC from different sources. These involve three separated primary BrC sources, including BB emissions, ~~fossil fuel~~FFs emissions from RCC and on-road vehicles (FFs-TRA), and a part of SOA which has light absorption property whereas other types of primary OA (POA) and SOA ~~is~~ are assumed to be purely scattering. In this study, BB source corresponds to open fire, household biomass burning and biofuel consumption emissions.

For the primary emissions, previous BrC simulations have substituted it with a proportion of POA directly (Feng et al., 2013; Lin et al., 2014; Wang et al., 2014; Tuccella et al., 2020; Xu et al., 2024) , derived it from the relationship between the burning efficiency and the observed aerosol light absorption (Jo et al., 2016; Zhu et al., 2021), or determined it through parameterization where BrC absorption is a function of the BC-to-OA emission ratio (Zhang et al., 2020). In the present work, we calculated the primary BrC emissions based on the bottom-up OA emission inventory combined with reported annual BrC emissions from various primary sources, as shown in Table 1. Firstly, we collected the reported annual emissions of BrC from RCC, BB and FFs-TRA by using bottom-up inventory method~~, as shown in Table 1~~. It should be noted that given the proximity of the study period (January 2014) to 2013, we use the emissions of BrC from RCC and BB in 2013 provided by Sun et al., (2017; 2021), which is 592Gg and 712Gg, respectively. The emissions of FFs-TRA derived BrC is 76Gg, which is calculated based on the value of 2017 (Wang et al., 2022a)and scaled by a factor of 0.70 to reflect the ~~ratio~~ change of annual

带格式的: 缩进: 首行缩进: 0 字符, 制表位: 不在 2 字符

设置了格式: 突出显示

设置了格式: 突出显示

设置了格式: 突出显示

设置了格式: 突出显示

设置了格式: 突出显示

设置了格式: 突出显示

设置了格式: 突出显示

设置了格式: 突出显示

设置了格式: 突出显示

设置了格式: 突出显示

设置了格式: 突出显示

设置了格式: 突出显示

设置了格式: 突出显示

civilian-owned motor vehicles. We assume that the spatial and seasonal variation of BrC is similar to OA. ~~T~~Then bottom-up emissions inventory ~~we~~ induced monthly BrC emissions in the NCP in January 2014 ~~by~~ is the annual BrC emissions multiplied~~ied~~ by the ratio of OA emissions ~~of~~ in NCP *vs* China, and the ~~R~~ ratio of OA emissions in January 2014 *vs* the whole year, resulting in a value of 65.5 Gg, 56.8 Gg and 4.4 Gg for RCC, BB and FFs-TRA, respectively. Finally, the proportion of the three primary emissions of BrC used in the model is 36.3%, 100.8% and 15.8%, respectively.

~~Up to now, the study for BrC emissions is limited (Sun et al., 2017; Sun et al., 2021; Wang et al., 2022b). Quantifying emission factors of BrC is still challenging due to the need to isolate BrC from other pollutants, and the factors vary greatly depending on the methods and proxies used. There are usually two methods to estimate the emissions of BrC, one is the traditional inventory method, and the other is calculating by using the ratio of BrC to other combustion products like BC. The gap between these two methods, even the same method, could be very wide. Sun et al., (2017; 2021) reported that the BrC from RCC and BB emission is 592 Gg and 712 Gg, respectively in 2013 in China but it likely to be biased low because of the proxy of BrC. Whereas Zhu et al., (2021)obtained a large RCC emissions (2.42 Tg year^{-1}) by using the emission ratio method. In the present work, we have taken consideration of the observation results that fossil sources significantly contribute to water soluble organic carbon (WSOC), especially in colder seasons, and that both the contribution and light absorption efficiency of WSOC are higher in northern China than in southern China (Feng et al., 2013; Mo et al., 2021). Follow on this study, we use a proportion of OA from different sources to estimate the emissions of BrC. RCC is responsible for about 45% of primary BrC emissions resulting in an annual emission of 616 Gg in the NCP. While all the BB emissions of OA are considered to be absorption, contributing approximately 45% to primary BrC emissions which is 664 Gg per year in NCP. The vehicle emissions of BrC is are based on the calculations made by Wang et al., (2022), and are about 84 Gg year^{-1} in this study. The total yearly BrC primary emissions in the NCP is over 1364 Gg year^{-1} which is closer to the estimation of traditional inventory method (加文献).~~

Figure 2 shows the contributing regions and burdens of the three separated primary sources of BrC. ~~图要改~~

设置了格式: 突出显示
设置了格式: 突出显示
设置了格式: 突出显示
设置了格式: 突出显示
设置了格式: 突出显示
设置了格式: 字体颜色: 自动设置
设置了格式: 突出显示

Table 1 The data for primary BrC emissions calculation

Primary sources of BrC	RCC	BB	FFs-TRA
Annual BrC emissions (Gg) in China	592.0[a]	712.0[b]	76.0[c]
Ratio of OA emissions in the NCP *vs* China[e]	57.7%	51.0%	69.4%
Ratio of OA emissions in January 2014 *vs* the whole year[e]	19.2%	14.0%	8.3%
Bottom-up emissions inventory induced monthly BrC emissions in the NCP in January	65.5	56.8[d]	4.4
Emissions in the NCP in January 2014[e]	180.2	56.4	27.9
BrC emissions ratio for primary sources used in the model	36.3%	100.8%	15.8%

[a] The BrC emissions from China's RCC in 2013 was reported by Sun et al., (2017) based on experiments involving seven coals were burned in four typical stoves as both chunk and briquette styles.

[b] The calculated BrC emissions from China's household biomass burning in 2013 reported by Sun et al., (2021) using 11 widely used biomass types in China burned in a typical stove.

[c] The estimated BrC emissions from vehicle exhaust in 2017 was 109 Gg reported by Wang et al., (2022a). In this study, the emissions of FFs-TRA derived BrC is 76.0 Gg with a yearly scale factor 0.70 which derived by the annual civilian-owned motor vehicles between 2014 and 2017.

[d] The value of BrC emissions in NCP in January 2014 is additionally added with OA emitted from the open-biomass burning (6 Gg) which is assumed to be entirely light-absorbing.

[e] These values were derived from the OA emission inventory described in Sec. 2.1

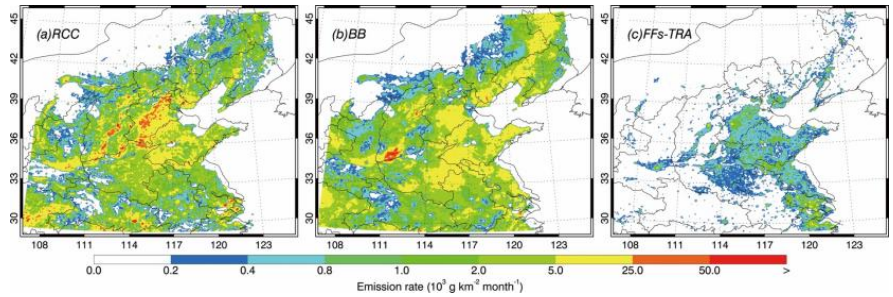

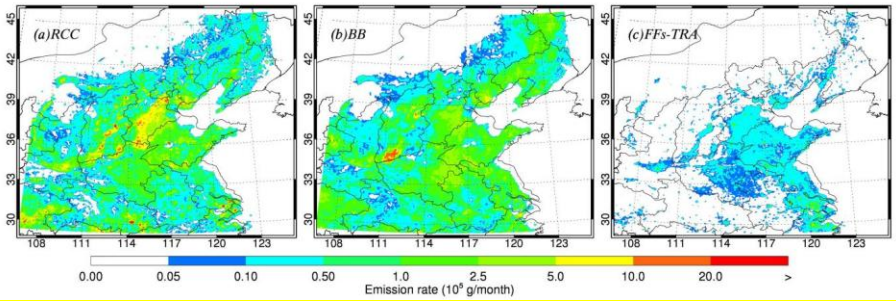

设置了格式: 突出显示
设置了格式: 突出显示
设置了格式: 突出显示
设置了格式: 突出显示
设置了格式: 突出显示
设置了格式: 突出显示
设置了格式: 突出显示

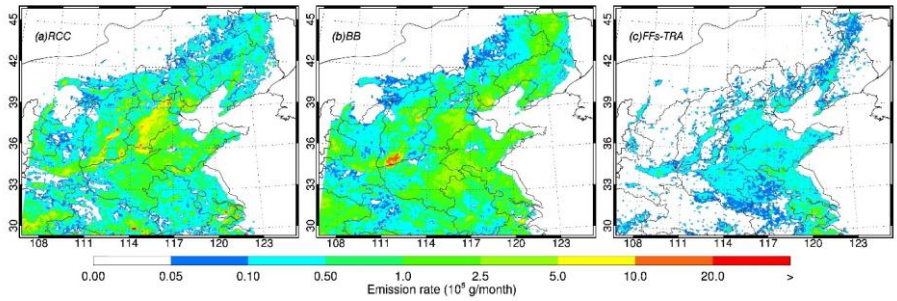

Figure 2 Monthly BrC emissions burdens in January 2014 in NCP from RCC, BB and FFs-TRA.

SOA has also shown light absorption in the atmosphere (Lin et al., 2014). Laboratory experiments have revealed that most of the light-absorbing SOA is associated with aromatic ~~carbonyls~~SOA (Jacobson, 1999; Laskin et al., 2015; Li et al., 2020) ~~文献~~ and the absorption from biogenic SOA in the field has been found to be negligible (Washenfelder et al., 2015) ~~文献~~. Therefore, ~~In this work,~~here ~~we~~ assume aromatic derived SOA ~~only secondary~~as secondary BrC in the model following previous studies (Jo et al., 2016; Wang et al., 2018).

Moreover, it is worth noting that both primary and SOA light absorption were shown to be dynamic, where BrC can be bleached when they undergo photodissociation (Forrister et al., 2015; Wong et al., 2019), or be darken by cloud and fog processing of aerosols (Moise et al., 2015; Lin et al., 2017; Cheng et al., 2020). These processes are not considered in this study yet. More detailed parameterization of the chemical aging of BrC are needed in future BrC models. ~~a proportion of 10% of the total SOA is included as a part of BrC. Applying the emission fractions above, OA is split into white scattering POA, white scattering SOA and BrC at each time step.~~

~~in[a]. [a]Bottom-up emissions inventory induced monthly [a]~~

~~[a] There values were derived from the OA emission inventory described in Sec. 2.1~~

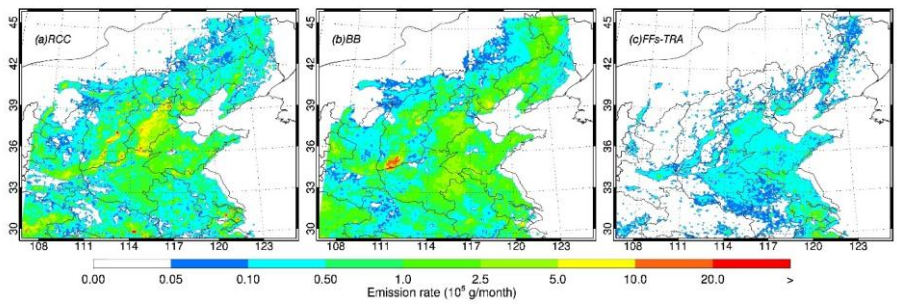

~~**Figure 2 Monthly BrC emissions burdens in January 2014 in NCP from FFs-coal, BB and FFs-traffic.**~~

设置了格式: 突出显示
设置了格式: 突出显示
设置了格式: 字体颜色: 文字 1, 突出显示
设置了格式: 字体颜色: 文字 1, 突出显示
设置了格式: 字体颜色: 文字 1, 突出显示
设置了格式: 字体颜色: 文字 1, 突出显示
设置了格式: 字体颜色: 文字 1
设置了格式: 字体颜色: 文字 1, 突出显示
设置了格式: 突出显示
设置了格式: 突出显示
设置了格式: 突出显示
设置了格式: 字体: 小五
设置了格式: 字体: 小五, 上标
带格式的: 缩进: 首行缩进: 0 字符

2.3.2 BrC optical properties

The refractive indices of BrC as a function of wavelength are used for radiative transfer calculations. The complex refractive index ($m = n + ik$) of aerosol components enables practical implementation in the model, where n is the real part primarily associated with the scattering efficiency ~~efficiency~~, and k is the imaginary part primarily associated with the absorption efficiency (Bohren and Huffman, 1998). The real part of BrC refractive index is the same of non-absorbing OA which is fairly constrained with reported values typically ranging from 1.5 to 1.7 (Saleh et al., 2014; Browne et al., 2019; Li et al., 2020). In this study, it follow the study by Li et al. (2011a) and Wu et al. (2020). The imaginary part (k) of BrC refractive index exhibit strong wavelength dependence and the values range over several orders of magnitude (Saleh et al., 2018; Sengupta et al., 2018) ~~(Saleh et al., 2018; Sengupta et al., 2018)~~. Limited studies on the optical properties of BrC from fossil fuel combustions are reported at present. The average mass absorption efficiency (MAE) of RCC at 365nm is ranging from 0.80 m^2 g^{-1} to 2.47 m^2 g^{-1} (Yan et al., 2017; Li et al., 2019; Tang et al., 2020; Wang et al., 2020; Ni et al., 2021; Song et al., 2021; Wang et al., 2021). In this study~~Here~~, as shown in Table 2, ~~we use~~ two sets of MAE are used for the sensitivity experiments of BrC. We choose a field optical measurement of BrC from all sources made by Zhang et al., (2022b)~~Zhang et .,~~ as the high absorption case (HI-BRC-ABS) .The optical properties of BB and FFs-TRA obtained in laboratory by Xie et al.,~~(Xie et al.,~~ (2017), as well as MAE of RCC and secondary BrC obtained in laboratory by Ni et al, (2021)~~(2021)~~ are adopted as the low absorption case (LOW-BRC-ABS) in the study. The imaginary part of the two cases have shown wavelength dependent light-absorption properties and the changes in anthropogenic emissions affect the optical properties of BrC. The imaginary part of both two cases are interpolated to 11 wavelengths to match the aerosol radiation calculation of Goddard module in WRF-Chem. ~~Considering that BrC has a high light absorption efficiency in northern China during cold season (Mo et al., 2021), we choose a field measurement of MAE in the wavelength range between 370 nm and 660 nm, showing that the changes in anthropogenic emissions affect the optical properties of BrC (Zhang et al., 2022b). This MAE is higher than that reported by Ni et al., (2021) and Xie et al., (2017) to implement the absorption of BrC. The MAE of SOA follows the suggestion made by Ni et al., (2021)(2021) .~~

The value of k in this work is derived from the measured MAE using the following Eq.(6~~1~~) (Liu et al., 2013; Lu et al., 2015) as shown in Table2: ~~:~~

$$k_{Brc,\lambda} = \frac{\rho \times \lambda \times MAE_{\lambda}}{4\pi}$$

(6~~1~~)

设置了格式: 突出显示

设置了格式: 突出显示

设置了格式: 突出显示

设置了格式: 突出显示

设置了格式: 突出显示

设置了格式: 突出显示

设置了格式: 突出显示

设置了格式: 突出显示

设置了格式: 突出显示

设置了格式: 突出显示

带格式的: 缩进: 首行缩进: 0 字符

Where MAE_λ ($m^2\ g^{-1}$) is the bulk mass absorption efficiency of BrC at the corresponding wavelength λ. ρ (g cm^{-3}) is the density of organic aerosols, which is assigned as 1.2 g cm^{-3} (Turpin and Lim, 2001) in this study. And the imaginary part of both two cases were interpolated to 11 wavelength to match the aerosol radiation calculation of Goddard module in WRF-Chem.

Table 1 2 The refractive index of BrC used in the model

Aerosols	Wavelength (nm)	k	References
BrC-RCC	370	0.1890	
	470	0.0608	
	520	0.0272	
	590	0.0173	
	660	0.0081	
BrC-BB	370	0.0587	
	470	0.0219	
	520	0.0120	Zhang Y, 2022
	590	0.0092	
	660	0.0046	
BrC-FFs-Tra	370	0.0509	
	470	0.0194	
	520	0.0085	
	590	0.0046	
	660	0.0018	
BrC-SOA	365	0.00490	Ni et al., 2021
	500	0.00070	

Aerosols	Wavelength (nm)	*k* values for HI-BRC-ABS	*k* values for LOW-BRC-ABS
BrC-RCC	365	-	0.0320
	370	0.1890	-
	470	0.0608	-
	500	-	0.0020
	520	0.0272	-
	590	0.0173	-
	660	0.0081	-
BrC-BB	365	-	0.0300
	370	0.0587	-
	405	-	0.0016
	470	0.0219	-
	520	0.0120	-
	550	-	0.0026
	590	0.0092	-
	660	0.0046	-
BrC-FFs-Tra	365	-	0.0180
	370	0.0509	-
	405	-	0.0130
	470	0.0194	-
	520	0.0085	-
	550	-	0.0045
	590	0.0046	-
	660	0.0018	-

设置了格式: 突出显示
设置了格式: 突出显示
设置了格式: 突出显示
设置了格式: 突出显示
设置了格式: 突出显示
设置了格式: 突出显示
设置了格式: 字体颜色: 文字 1, 突出显示
带格式的: 行距: 多倍行距 0.95 字行, 不对齐到网格
设置了格式: 字体颜色: 文字 1, 突出显示
设置了格式: 字体颜色: 文字 1, 突出显示
设置了格式: 字体颜色: 文字 1, 突出显示
设置了格式: 字体颜色: 文字 1, 突出显示
设置了格式: 字体颜色: 文字 1, 突出显示
带格式的: 行距: 多倍行距 0.95 字行, 不对齐到网格
设置了格式: 字体颜色: 文字 1, 突出显示
带格式的: 行距: 多倍行距 0.95 字行, 不对齐到网格
设置了格式: 字体颜色: 文字 1, 突出显示
带格式的: 行距: 多倍行距 0.95 字行, 不对齐到网格

BrC-SOA	365	-	0.0049
	370	0.0251	-
	470	0.0166	-
	500	-	0.0007
	520	0.0114	-
	590	0.0107	-
	660	0.0063	-

'-' means not available

2.3.3 Shortwave direct radiative effect calculation and experimental design

The shortwave DRE calculations of BrC follow the method reported by Chen et al (2021) as shown in Eq. (7~~2~~). The DRE of BrC is calculated by the difference between the net radiant flux with and without BrC, where the net radiant flux is the difference between the downward ($F_{\downarrow}$) and upward radiant flux ($F_{\uparrow}$).

$$DRE_{TOA} = (F^{a}_{\downarrow TOA} - F^{a}_{\uparrow TOA}) - (F^{0}_{\downarrow TOA} - F^{0}_{\uparrow TOA}) \quad (7~~2~~)$$

Where DRE_{TOA} represent the shortwave DRE at the top of the atmosphere (TOA). F^{a} and F^{0} ~~is~~ are the radiant flux with and without BrC aerosols, respectively.

An adjoint methodology proposed by Zhao et al (2013) and Huang et al. (2015) has been used to diagnose the optical depth and DRE of BrC aerosols. Optical properties and radiative transfer of different sources BrC are calculated multiple times with one or a group of aerosol mass removed or without BrC absorption from each ~~of~~ calculation ~~as the~~ following Eq. (8~~3~~) and Eq. (9~~4~~). In addition, the model also takes into account the reduced aerosol masses along with the change in aerosol number concentration and size distribution.

$$AOD_{[species\ i]} = AOD_{[all\ species]} - AOD_{[without\ species\ i/without\ species\ i\ absorption]} \quad (8~~3~~)$$

$$DRE\ Forcing_{[species\ i]} = DRE\ Forcing_{[all\ species]} - DRE\ Forcing_{[without\ species\ i/without\ speices\ i\ absorption]} \quad (9~~4~~)$$

This method is more efficient than the traditional approach of running the model multiple times with the exclusion of a specific aerosol component. It not only saves computational time but also provides a more accurate estimation focused solely on the direct radiative effect of aerosols.

3 Results and Discussions

3.1 Model performance

Before evaluating the DRE of BrC ~~further~~, results from the standard simulation are used to validate the model performance. Using available measurements, we first validate the spatial distribution and temporal variation of air pollutants ($PM_{2.5}$, O_3, NO_2, SO_2) in the NCP, the temporal variation of downward shortwave flux at the surface (SWDOWN) in Beijing, Tianjin, Zhengzhou, Hefei and Ji'nan, and the temporal variation of aerosol species (OA,

设置了格式: 字体颜色: 文字 1, 突出显示
带格式的: 行距: 多倍行距 0.95 字行, 不对齐到网格
设置了格式: 字体颜色: 文字 1
设置了格式: 字体: (中文) 等线, 小五, 字体颜色: 文字 1, 突出显示
带格式的: 正文, 行距: 多倍行距 0.95 字行, 不对齐到网格
设置了格式: 突出显示
设置了格式: 突出显示

elemental carbon, ammonium, sulphate and nitrite) in Beijing and, Tianjin and of primary OA from BB, RCC, motor vehicles and SOA in Beijing in January, 2014. Detailed data descriptions and quantitative statements of model biases can be found in supplementary text S2.1 and S3. In general, the model simulates reasonably well ~~simulates~~ the air pollutants, SWDOWN, and aerosol species against measurements.

SSA determines the strength of aerosols in absorbing solar radiation. Here we conduct three sensitivity experiments to evaluate the effect of BrC with different *k* values on the simulated aerosol absorption. The first experiment is the control simulation in which all organic aerosols are treated as purely scattering particles with no absorption contribution of BrC, which is referred to as NOBRC. The hi-absorption scenario (HI-BRC-ABS) and low-absorption scenario (LOW-BRC-ABS) characterize BrC light absorption by using the higher and lower imaginary refractive index derived from Section 2.3.2, respectively. Figure 3 shows the comparisons of simulated versus observed SSA at 440 nm (SSA_{440}) at Sun-sky radiometer Observation NETwork (SONET) sites in Beijing, Songshan, Xi'an, Hefei, Nanjing in January 2014. Due to the influence of clouds, the observational data from SONET are not continuous, resulting in a total of 237 valid data points are available for comparison. Moreover, SSA retrieval typically have larger uncertainties at low AOD values (Dubovik et al., 2002). Therefore, we have excluded the SSA data when AOD is less than 0.5, which has 206 valid points in each case. We find that the inclusion of BrC in the model reduces the bias of simulated SSA. The HI-BRC-ABS case demonstrated a largest improvement with the correlation coefficient increasing to 0.54, making it the best simulation in the study. It suggests that stronger BrC absorption case, as prescribed in HI-BRC-ABS, better captures the aerosol optical properties observed in northern China during winter. Consequently, the HI-BRC-ABS case can serve as the the base simulation for further investigation of radiative effects of BrC in this study. Overall, the model tends to underestimate SSA_{440}. The underestimation might be partly caused by the overestimation of absorbing aerosols like BC or dust. Meanwhile, the uncertainties of the simulated SSA can be caused by other factors, such as mixing state of aerosols, particle shape, wavelength, and mass ration of non-black carbon to BC (Liu et al., 2017; Jeong et al., 2020).

设置了格式: 突出显示
设置了格式: 突出显示
设置了格式: 突出显示
设置了格式: 突出显示
设置了格式: 突出显示
设置了格式: 突出显示
设置了格式: 突出显示
设置了格式: 突出显示
设置了格式: 突出显示
设置了格式: 突出显示
设置了格式: 突出显示
设置了格式: 突出显示
设置了格式: 突出显示
设置了格式: 突出显示
设置了格式: 非突出显示
设置了格式: 突出显示
设置了格式: 突出显示
设置了格式: 突出显示
设置了格式: 突出显示
设置了格式: 突出显示
设置了格式: 突出显示

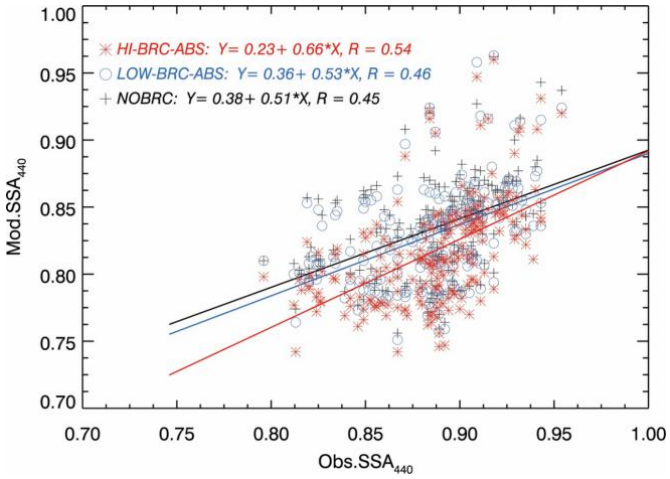

Figure 3. Scatter plot and linear fitting of modelled and observed column integrated SSA at 440 nm in case HI-BRC-ABS (red), LOW-BRC-ABS (blue) and NOBRC (black) case.

The daily AOD at 550 nm (AOD_{550}) from the dataset of Long-term Gap-free High-resolution Air Pollutant (LGHAP), derived via tensor-flow-based multimodal data fusion method (Bai et al., 2022), is compared with the simulation. This gap-free daily AOD dataset at 1 km resolution for 2000–2020 in China was generated by integrating multimodal data from satellites, numerical models, and in situ measurements. Data gaps in Moderate Resolution Imaging Spectroradiometer (MODIS) AOD are reconstructed through spatial pattern recognition and statistical knowledge transfer. Validation against Aerosol Robotic Network (AERONET) observations showed strong agreement, with an R of 0.91 and an RMSE of 0.21. Figure 43a and 43b shows the pattern comparison of the monthly simulated and retrieved AOD_{550}. The model ~~reasonably~~ reproduces the retrieved AOD distribution ~~compared to the retrieval~~ in the NCP reasonably~~, but slightly underestimates the AOD_{550}~~. The monthly average simulated and retrieved AOD_{550} is 0.45 and 0.48 on average in the NCP, respectively. Figure 3c shows the scatter plot of the daily simulated and retrieved AOD_{550} averaged in the NCP during the simulation period. The simulated daily average AOD_{550} correlates quite well with the retrieved value~~val~~, with a regression slope of 1.085 and correlation coefficient of 0.832. Generally, the retrieved and simulated AOD increases with deterioration of the particulate pollution. Figure 45 provides the pattern comparison of the simulated and Ozone Monitoring Instrument (OMI) retrieved AOD at 440 nm (AOD_{440}) averaged during the simulated episode. OMI aboard NASA's Aura satellite offers global atmospheric measurements at a spatial resolution of 0.25°×0.25°, with

设置了格式: 字体颜色: 自动设置

设置了格式: 英语(英国)

设置了格式: 字体: (中文) +中文正文 (等线), 10 磅, 字体颜色: 自动设置, 突出显示

设置了格式: 字体: (中文) +中文正文 (等线), 10 磅, 字体颜色: 自动设置, 突出显示

设置了格式: 突出显示

设置了格式: 字体: (中文) +中文正文 (等线), 10 磅, 字体颜色: 自动设置, 突出显示

设置了格式: 字体: (中文) +中文正文 (等线), 10 磅, 字体颜色: 自动设置, 突出显示

设置了格式: 突出显示

设置了格式: 突出显示

设置了格式: 突出显示

设置了格式: 突出显示

Beijing's overpass occurring at approximately 13:45 local time. The averaged ~~simulated~~ AOD_{440} from the model simulation at 1~~4~~3:00 local time show~~spattern is~~ generally ~~in~~ agreement with the OMI retrieval~~, but the underestimation still exists~~. The average simulated and retrieved AOD_{440} is 0.51~~0~~ and 0.53 in the NCP, respectively. Overall~~In brief~~, the model generally performs well in simulating the AOD distribution~~, but is subject to underestimating AOD~~. It is worth noting that the simulated AOD is not only dependent on the column aerosol content and composition, but is also substantially influenced by relative humidity (RH) which determines the aerosol hyg~~d~~roscopic growth. Additionally, the satellite retrieved AOD is subject to contamination by the presence ~~existence~~ of clouds, and considering the high occurrence frequency of clouds during haze days, the retrieved AOD might be overestimated ~~is generally higher than the simulation~~ (Satheesh et al., 2010; Chand et al., 2012).

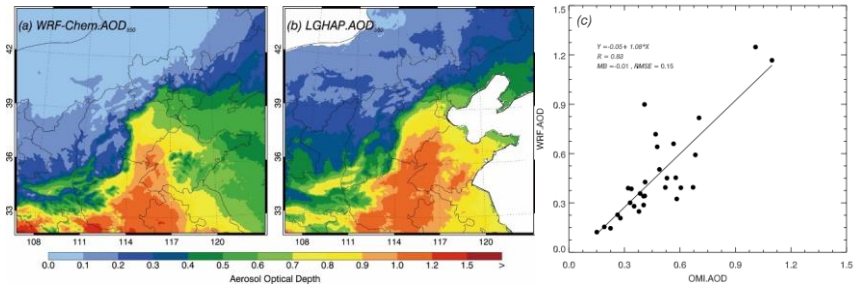

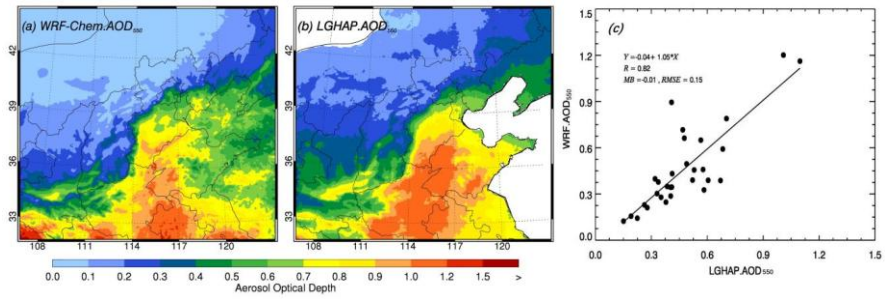

Figure 4~~3~~ (a) monthly simulated AOD_{550} of WRF-Chem, (b) monthly retrieved AOD_{550} of reanalysis dataset LGHAP, and (c) scatter plot of the daily simulated and retrieved AOD_{550} averaged in the NCP from 01 January to 30 January

设置了格式: 突出显示
设置了格式: 突出显示
设置了格式: 突出显示
设置了格式: 突出显示
设置了格式: 突出显示
设置了格式: 突出显示
设置了格式: 突出显示
设置了格式: 突出显示
设置了格式: 突出显示
域代码已更改
设置了格式: 字体: (中文) Times New Roman, 小五, 加粗, 英语(英国)
带格式的: 题注, 段落间距段后: 10 磅, 制表位: 不在 2 字符
设置了格式: 字体: (默认) Times New Roman, (中文) Times New Roman, 小五, 加粗
设置了格式: 字体: (默认) Times New Roman, (中文) Times New Roman, 小五, 加粗, 英语(英国)
设置了格式: 字体: (默认) Times New Roman, (中文) Times New Roman, 小五, 加粗
设置了格式: 字体: (默认) Times New Roman, (中文) Times New Roman, 小五, 加粗, 英语(英国)
设置了格式: 字体: (默认) Times New Roman, (中文) Times New Roman, 小五, 加粗
设置了格式: 字体: (默认) Times New Roman, (中文) Times New Roman, 小五, 加粗, 英语(英国)
设置了格式: 字体: (默认) Times New Roman, (中文) Times New Roman, 小五, 加粗

2014

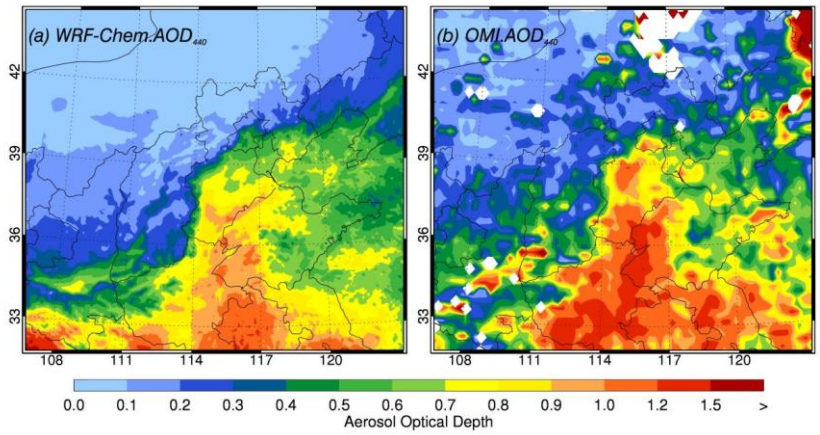

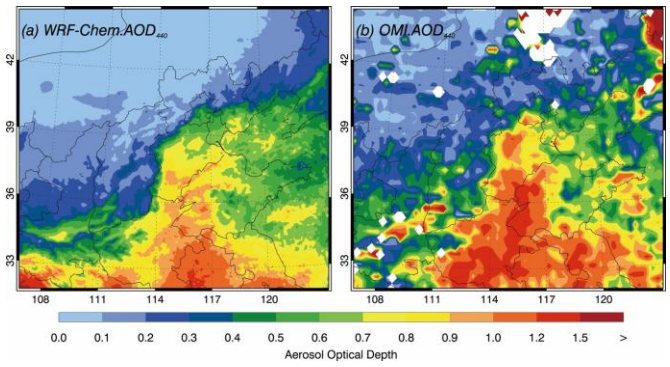

Figure 54 (a) monthly simulated AOD_{440} of WRF-Chem, (b) monthly retrieved AOD_{440} of OMI in the NCP from 01 January to 30 January 2014

~~SSA determines the strength of aerosols in absorbing solar radiation. Figure 5 shows the comparisons of simulated versus observed SSA at 440 nm (SSA_{440}) at Sun-sky radiometer Observation NETwork (SONET) sites including Beijing, Songshan, Xi'an, Hefei, Nanjing in January 2014. Due to the influence of clouds, the observational data from SONET are not continuous, consequently, a total of 237 valid data points are available for comparison. The model tends to underestimate SSA_{440} with a MB of -0.04. The relationship indicates that the model might predict more absorbing aerosols or underestimate RH. Meanwhile, the uncertainties of the simulated SSA can be caused by other factors, such as mixing state of aerosols, particle shape, wavelength, and mass ration~~

~~of non-black carbon to BC (Liu et al., 2017). Jeong et al. (2020) have proposed that the density of BC is an important factor for the SSA estimation, and dust size distribution reduces SSA_{440}.~~

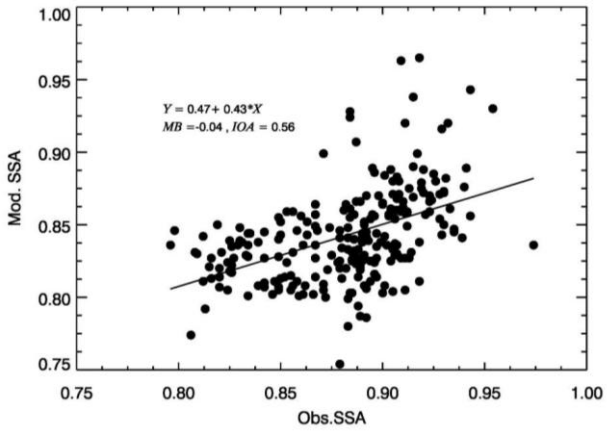

~~**Figure 5. Scatter plot and liner fitting of column integrated SSA at 440 nm.**~~

3.2 Surface mass concentrations of BrC in NCP

The simulated distribution of average near-surface BrC concentrations and each source contribution in January 2014 is shown in Fig. 6a. In January, the monthly mean concentrations of BrC in the NCP vary from 0.05 μg m^{-3} to ~~39.0~~42.3~~40.8~~ μg m^{-3}, with an average of ~~4.8~~5.2 μg m^{-3}. The spatial distribution of near-surface BrC concentrations is like that of $PM_{2.5}$ in the NCP, with the highest concentration areas located in Hebei Province with an average concentration of ~~13.6~~14.9~~5~~ μg m^{-3}. The simulated BrC concentrations are higher than those reported by Zhu et al.(Bai et al., 2022; Zhu et al., 2021) ~~(2021)~~ (2021) in 2018, which is perhaps caused by the more severe particulate pollution in January 2014. ~~2014.~~

设置了格式: 非突出显示

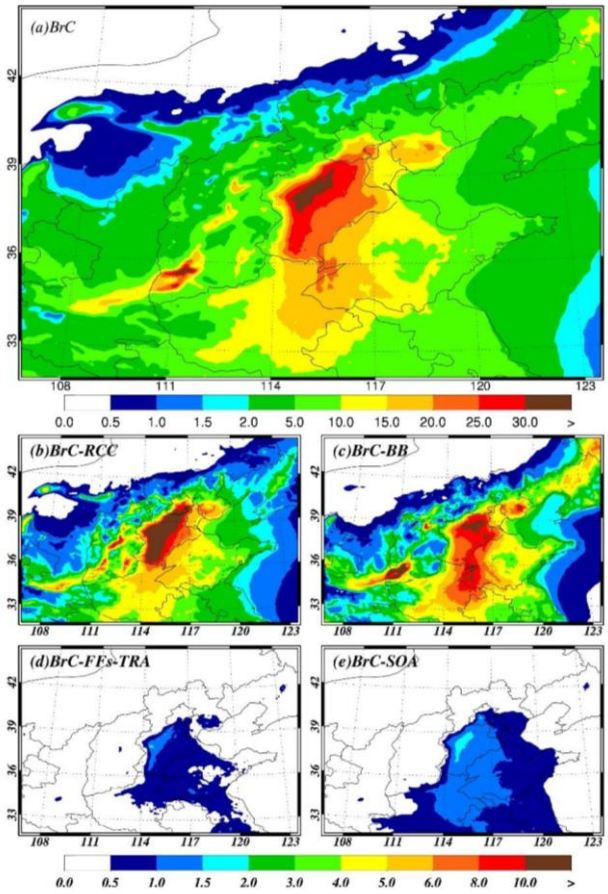

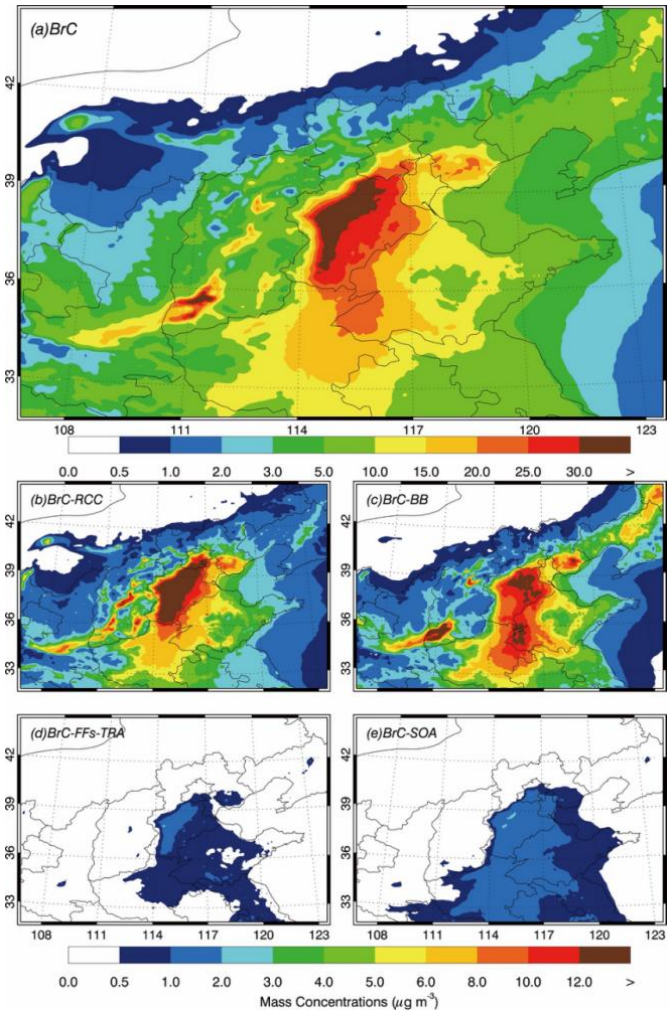

357

358

带格式的: 居中, 缩进: 首行缩进: 0 字符

带格式的: 居中, 缩进: 首行缩进: 0 字符

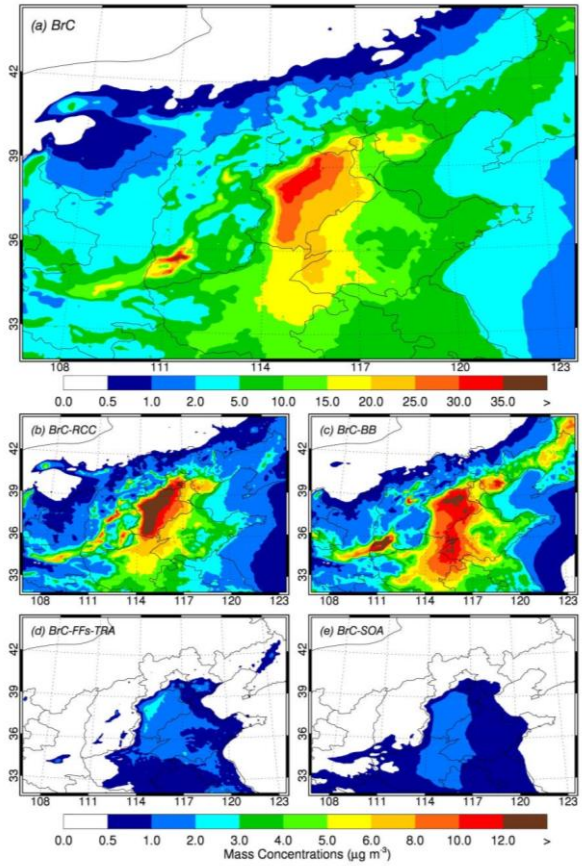

Figure 6. Simulated mean surface concentrations of BrC (a) and contributions from ~~each anthropogenic source of~~ RCC (b), ~~of~~ BB (c), ~~of~~ FFs-TRA (d) and secondary BrC (e) in January 2014 in NCP

Figure 6b-e present the average near-surface BrC concentrations from different anthropogenic sources and secondary formation in January 2014 in the NCP. The BrC in the NCP predominantly originates from RCC and BB, with an average contribution of 2.3 and 2.49 μg m^{-3} and a maximum of ~~28.23~~1.93.8 and 31.629.0~~31.3~~ μg m^{-3}, respectively. A relatively small proportion of BrC is ~~contributed by~~related to FFs-TRA and secondary transformations with an average concentration of 0.25~~ μg m^{-3} and 0.434 μg m^{-3}, respectively. The BrC from RCC accounts for 5456.83% of total BrC concentrations in the NCP, which is highest in Beijing, Hebei, and Tianjin, reaching 6783.72%, 4854.45.50% and 53.3447.17% respectively. The BrC from BB counts 36.941.9% of total BrC concentrations, with ~~the~~ a contribution of about 40% in most provinces of the NCP but only 26.58.9% in

带格式的: 缩进: 首行缩进: 0 字符

带格式的: Citavi Bibliography Entry, 段落间距段后: 0 磅, 行距: 1.5 倍行距, 制表位: 2.03 字符, 左对齐

设置了格式: 突出显示

设置了格式: 突出显示

设置了格式: 突出显示

设置了格式: 突出显示

Beijing. This result shows that the RCC is one of the major sources of BrC in NCP due to the wide use of coal for heating and cooking in winter with ~~the~~ low combustion efficiency and ~~fewer~~ little emission control. The BrC emitted by RCC is mainly concentrated in the Beijing-Tianjin-Hebei (BTH) region in January 2014, while the BrC emitted by BB is distributed in the whole NCP. The Fen-Wei plain exhibits notably high contributions from BB, which is consistent with the emission distribution and with previous studies (Cao and Cui, 2021; Zhang et al., 2021). The Fen-Wei Plain is one of the most densely populated and heavily polluted areas in northern China where biomass is usually used for heating during winter. ~~Although the BrC concentration from FFs-TRA is generally higher in Hebei Province than that in other regions, the highest BrC contribution from FFs-TRA is in Jiangsu Province, reaching up to 16.9%, with an average of 6.1%.~~

3.3 BrC absorption in the NCP

BrC absorbs visible to near-ultraviolet light with its absorption capabilities extending prominently at shorter wavelengths. Therefore, we calculate the AAOD (aerosol absorption optical depth) to evaluate the absorption contribution of BrC versus bulk aerosols, each anthropogenic source and SOA versus BrC at 365 nm (Fig. 7), by differentiating the AAOD between the model runs with and without the contribution of BrC ~~model runs~~. The average contribution of BrC to the total AAOD of aerosols at 365 nm is ~~11.2~~16.4% and the maximum is ~~33.6~~9.5% in the NCP in January 2014. The BrC to BC and OC ratios in surface air in the study is 2.2 and 0.31, respectively~~,~~, ~~and~~They are higher than the surface ratio used in the global models (Jo et al., 2016; Park et al., 2010) ~~(Jo, Park)~~, but lower than the ratio of Feng et al., ~~2013~~(2013). Although~~t~~ the concentrations of BrC is relatively high and ~~Compared with the global mean ratio of BrC to BC which is 1.24 (Jo et al., 2016),, the near-surface~~ BrC to BC ratio ~~of that~~determined for ~~in the NCP is relatively low, with an average of 0.85, resulting from the~~ ~~because of high concentrations of BC in this area. It~~ This ratio is also much lower than that found ~~in South America and Africa where BB~~ emissions ~~is generally heavy (Jo et al., 2016). On the other hand, although~~ the absorption of BrC in the ultraviolet band is comparable to that of BC, ~~but~~ the imaginary index of BrC (about 0.1) is still much lower than that of BC (about 0.76). As a result, the light absorption contribution of BrC at 365 nm is not as significant during the study period.

Furthermore, the light absorption properties of BrC during the winter season are predominantly attributed to RCC, followed by BB, SOA, and FFs-TRA in the NCP. The average contribution of RCC and BB to the AAOD of BrC is 5~~9~~5.3% and 2~~6.4~~6.3%, respectively. Although the concentration of BrC from RCC is comparable to that from BB, the much higher light-absorbing property of the BrC from RCC makes it a dominant contributor to the

设置了格式: 突出显示
设置了格式: 突出显示
设置了格式: 突出显示
设置了格式: 突出显示
设置了格式: 突出显示
设置了格式: 突出显示
设置了格式: 突出显示
设置了格式: 突出显示
设置了格式: 突出显示
设置了格式: 突出显示

overall light absorption caused by BrC. ~~The concentration of secondary BrC is lowest lower compared to that from primary sources, but contributes considerably to BrC AAOD with an average up to 10.6%~~ Despite lower surface concentrations compared to primary BrC, secondary BrC contributes significantly to AAOD of BrC, averaging ~10.0% with elevated contributions in the sea and remote regions, which is likely due to the highly oxidized character of organic aerosols and its chemical aging in aging air masses leading to the formation of BrC (Gouw et al., 2005; Kawamura et al., 2005; Tsigaridis and Kanakidou, 2018). While AOD represents column-integrated concentrations, the secondary BrC to Primary BrC ratio increases from 8.9% at the surface to 12.0% of atmospheric burden. It reaches 14.3% at an altitude of 500m as shown in Figure S6, which could lead to a higher absorption contribution of secondary BrC (Wang et al., 2022b). Moreover, the observations indicate that a substantial SOA is water-soluble (Maria et al., 2003; Peng et al., 2021) which is treated as hygroscopic components in the model and its absorption could be magnified. ~~, which could be explained by its low density and mixing state.~~ The AAOD contribution of BrC from vehicles ~~sources~~ is the lowest, about ~~3~~1.8% on average, but its contribution in ~~Shanghai and~~ southern Jiangsu and southeast Anhui ranges from ~~4~~5% to ~~8~~10%, higher than in other regions~~, which is consistent with the its surface mass concentration distribution.~~ . This may suggest that motor vehicle emissions account for a significant proportion of pollution in this area.

设置了格式: 突出显示

设置了格式: 突出显示

设置了格式: 突出显示

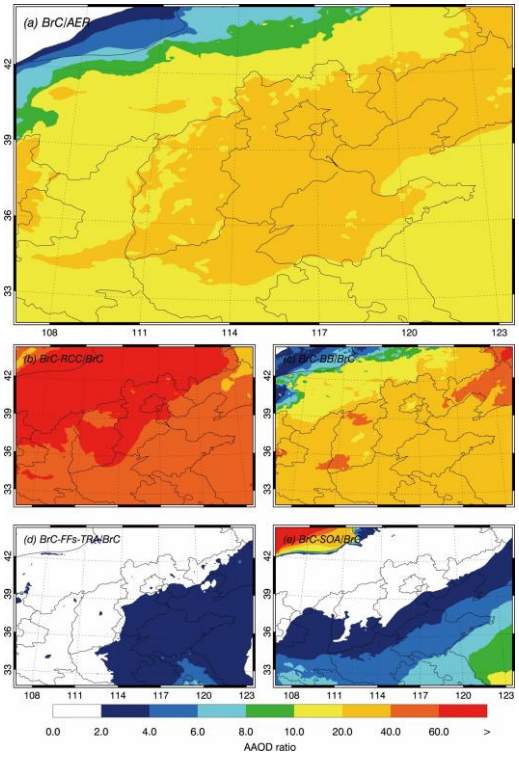
(a) BrC/AER
(b) BrC-RCC/BrC
(c) BrC-BB/BrC
(d) BrC-FFs-TRA/BrC
(e) BrC-SOA/BrC
42
39
36
33
108
111
114
117
120
123
0.0
2.0
4.0
6.0
8.0
10.0
20.0
40.0
60.0
>
AAOD ratio

414

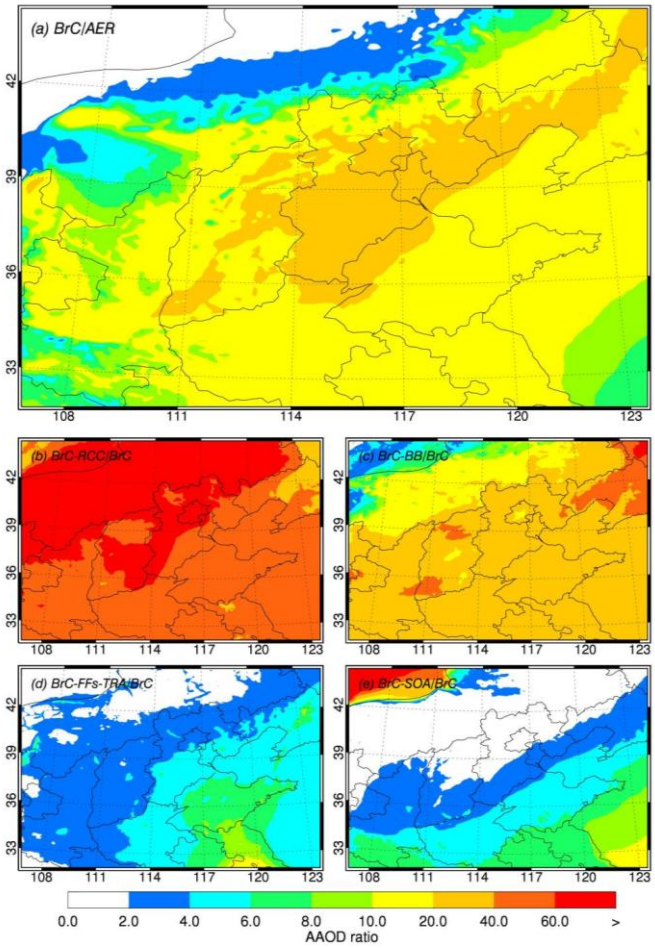

Figure 7 ~~S~~~~The s~~imulated monthly BrC AAOD versus aerosol at 365nm (a) and each anthropogenic source of RCC (b), BB(c), FFs-TRA (d) and secondary BrC (d) AAOD versus BrC in NCP

设置了格式: 突出显示

3.4 Direct radiative effect of BrC

Figure. 8a shows the distribution of the average DRE_{TOA} caused by BrC at the top of the atmosphere during the episode. The DRE_{TOA} of BrC in the NCP is -0.~~1~~009 W m^{-2} on average, with a maximum of +0.465 W m^{-2} and a minimum of -2.4~~5~~74 W m^{-2}. Compared to the average DRE_{TOA} of BC +3.9 W m^{-2} and a maximum of +21.6 W m^{-2}, the average DRE_{TOA} of BrC in the NCP is close to zero. However, in terms of the spatial distribution, the DRE_{TOA} of total BrC in the NCP is predominantly negative, especially in those areas with high BrC concentrations

设置了格式: 突出显示

设置了格式: 突出显示

including BTH area and Fen-wei Plain. The largest negative DRE_{TOA} is in Shanxi province, ~~where the with the~~ highest ~~BrC concentration produced by~~contributor to BrC is ~~–~~ BB. ~~The results indicate that the~~ overall scattering effect of BrC is greater than its absorption effect, ~~so~~ that ~~the~~ BrC ~~populations~~ have a net cooling effect. ~~As we know, t~~The solar irradiance in the UV band contributes only 10% ~~for~~ of the total solar irradiation~~. T~~ and the imaginary refractive indices of BrC are much lower than those strongly absorbing BC, especially in the visible band. On the other hand, although ~~these reasons~~this leads to a small heating effect by BrC, the increased DRE_{TOA} induced by BrC which is usually considered as its scattering effect, is up to an average of +0.40~~37~~ W m^{-2} and a maximum of +1.83~~2.45~~ W m^{-2} as shown in Fig. 8b. The DRE_{TOA} of OA without BrC is -2.00 W m^{-2} over the NCP (Fig. 8d) and is increased to -1.60~~3~~ W m^{-2} (Fig. 8c) after considering BrC. Consequently, the cooling effect of OA is reduced by BrC ~~with~~ by an average of 2~~4~~8.0%. So far, almost all estimates of the radiation effects of BrC have been based on a global basis. The study of Wang et al. (2014) ~~have shown that~~reported a ~~the~~ global DRE_{TOA} of BrC ~~of~~is -0.02 W m^{-2}, resulting in a DRE_{TOA} increas~~ing~~e of +0.07 W m^{-2}. Brown et al. (2018) have also reported a global annual increased DRE_{TOA} of +0.13 W m^{-2}, ~~–~~with the maximum forcing (~+1.75 W m^{-2}) occurring at~~s off~~ the west coast of southern Africa. ~~As a result, BrC reduces the cooling effect caused by organic aerosols by approximately 16%~~ (Jo et al., 2016). ~~However, A~~all these estimates only considered BB, biofuels or SOA. ~~This result indicate the solar radiation changes caused by BrC in NCP is notebaly and that the~~ and the significance of BrC ~~becomes apparent~~ in the estimates for ~~those~~ these studies~~y~~ typically based on the assumption that OA primarily scatters sun light. Our results indicate that the solar radiation changes caused by BrC in NCP is notable. The absorption effect of BrC should be considered in climate models to accurately assess the aerosol impact on atmospheric heating and climate change.

设置了格式: 突出显示
设置了格式: 突出显示
设置了格式: 突出显示
设置了格式: 突出显示
设置了格式: 突出显示
设置了格式: 突出显示
设置了格式: 突出显示
设置了格式: 突出显示
设置了格式: 突出显示
设置了格式: 突出显示
设置了格式: 突出显示
设置了格式: 字体颜色: 文字 1
设置了格式: 突出显示
设置了格式: 突出显示

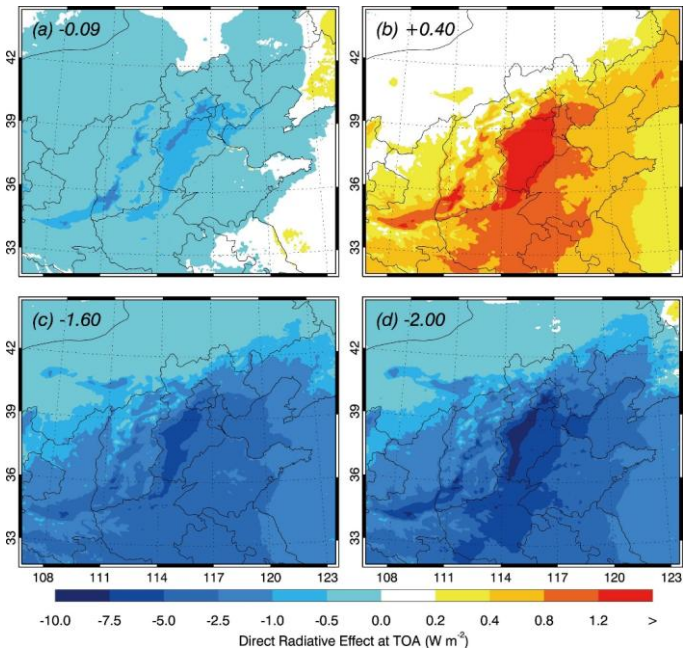

444

445

带格式的: 居中, 缩进: 首行缩进: 0 字符

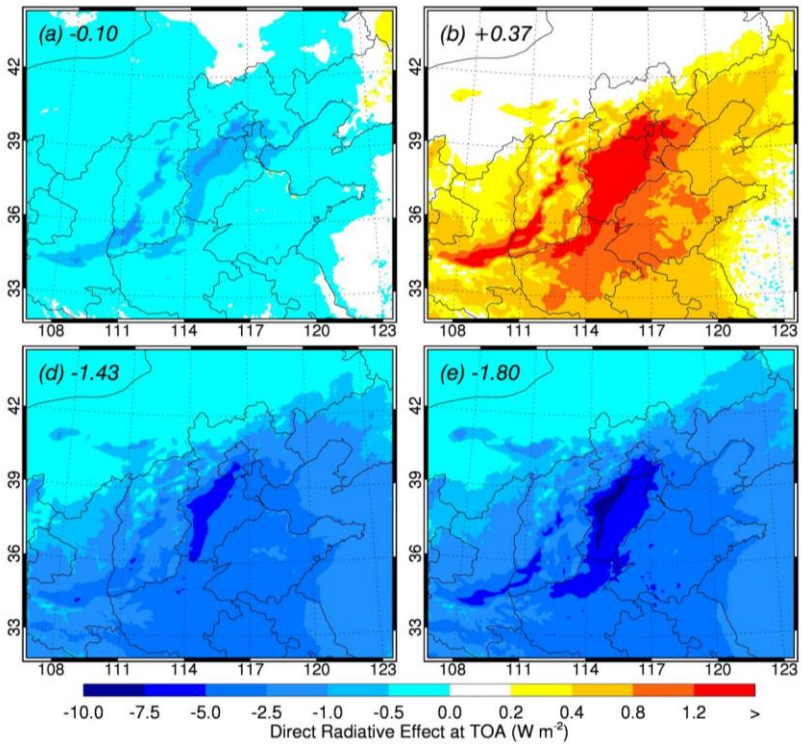
(a) -0.10
(b) +0.37
(d) -1.43
(e) -1.80
42
39
36
33
108
111
114
117
120
123
-10.0
-7.5
-5.0
-2.5
-1.0
-0.5
0.0
0.2
0.4
0.8
1.2
>
Direct Radiative Effect at TOA (W m-2)

446

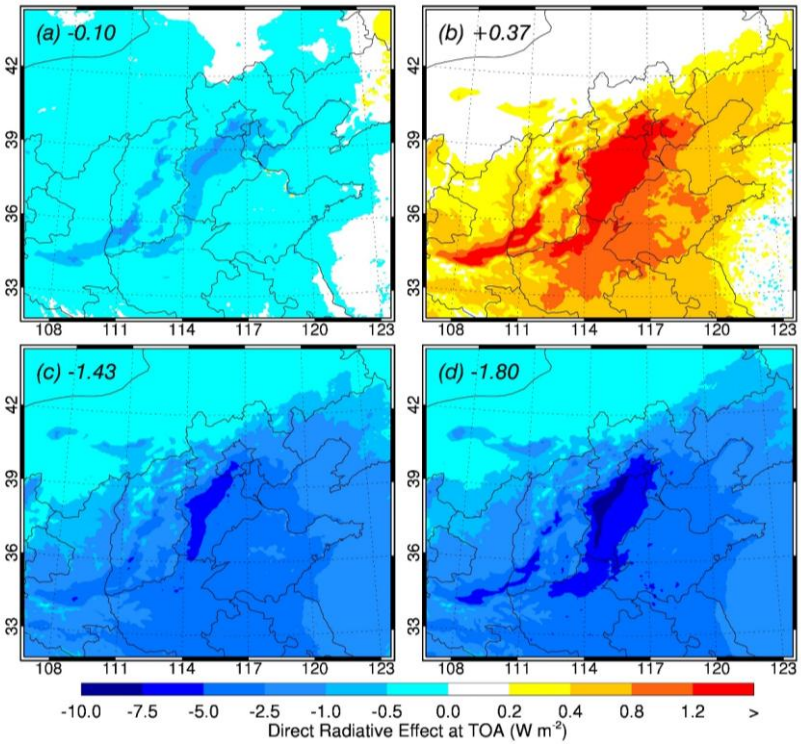

Figure 8, ~~The~~ Estimated DRE_{TOA} of BrC (a) and ~~the~~ DRE_{TOA} increase of OA owing to the absorption of BrC (b). The DRE_{TOA} of total OA with absorbing BrC (c) and DRE_{TOA} of total OA with BrC is assumed to be scattering (d). The averages of DRE are shown in the upper left of each panel.

Figure 9a-d shows the estimated DRE_{TOA} of BrC from RCC, BB, FFs-TRA and secondary BrC in the NCP during the episode. Similar to the contribution of BrC sources to the AAOD at 365 nm, the most important source contributing to DRE_{TOA} of BrC is RCC (+0.26~~0~~ W m^{-2}), followed by BB (+0.11 W m^{-2}), secondary BrC (+0.02 W m^{-2}), and FFs-TRA (+0.01 W m^{-2}) in the NCP, as shown in Fig. 9. ~~However~~In addition, the DRE_{TOA} of BrC from various sources exhibits distinct spatial distribution characteristics in the NCP. The highest DRE_{TOA} of BrC from fossil sources, which include RCC and FFs-TRA, are predominantly ~~appeared~~ concentrated in Hebei. The highest positive DRE_{TOA} of BrC from BB is found in Fen-Wei Plain. Meanwhile, the secondary BrC contributes most to the DRE_{TOA} in the south part of the NCP. The persistent high values over southern China might stem from the model's representation of secondary BrC as hygroscopic components (Peng et al., 2021), whose light-absorbing capacity is amplified in the region with high ambient humidity ~~properties~~.

设置了格式: 突出显示

461

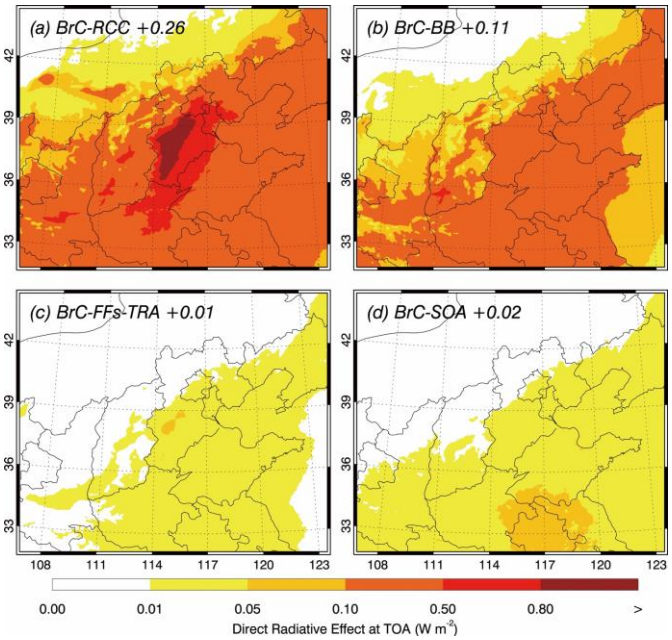
(a) BrC-RCC +0.26
(b) BrC-BB +0.11
(c) BrC-FFs-TRA +0.01
(d) BrC-SOA +0.02
42
39
36
33
108
111
114
117
120
123
0.00
0.01
0.05
0.10
0.50
0.80
>
Direct Radiative Effect at TOA (W m-2)

462

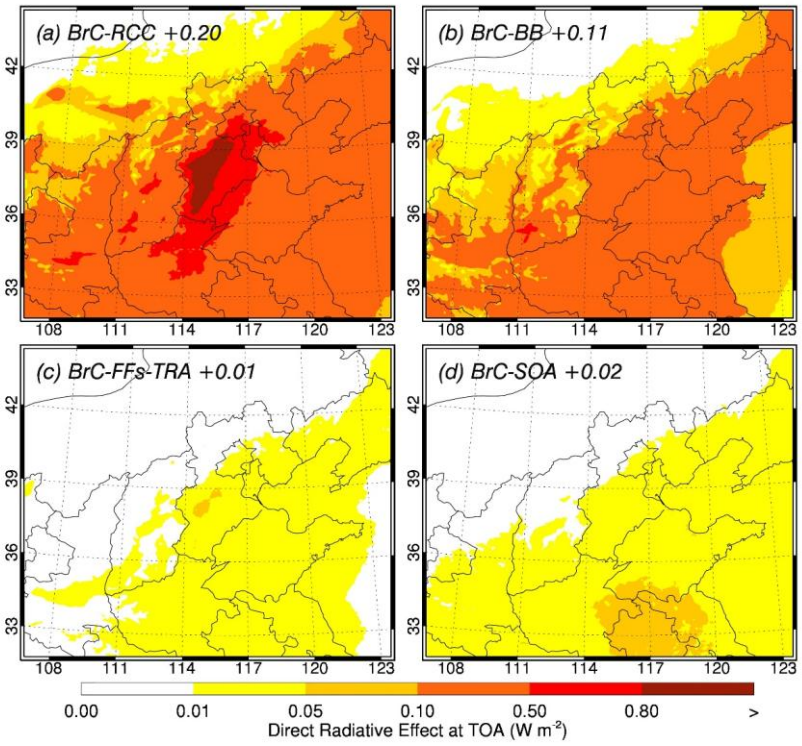

463

带格式的: 正文, 段落间距段前: 自动, 段后: 自动, 制表位: 不在 2 字符

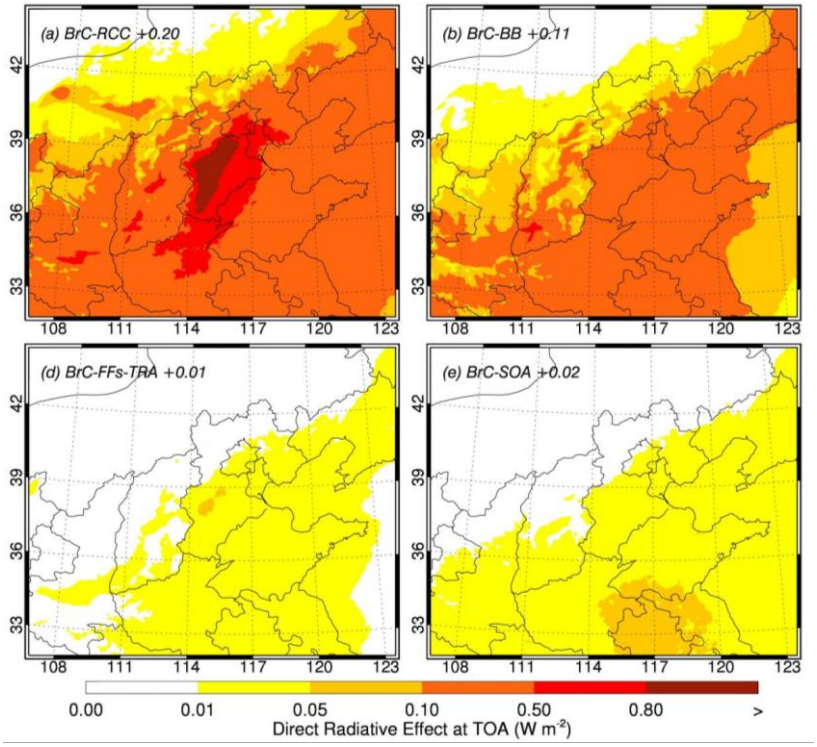

Figure 9. The estimation DRE_{TOA} of BrC from each anthropogenic source ~~(a)~~RCC(a), ~~(b)~~BB(b), ~~(c)~~ FFs-TRA(c) and ~~(d)~~ secondary BrC(d) in NCP in January 2014

4 Conclusions

A source-explicit BrC simulation in January 2014 in the NCP is conducted by using the WRF-Chem model. We define the BrC based on varying proportions of RCC, BB, FFs-TRA and SOA sources, assigning each a distinct imaginary refractive index to represent their differing light absorption characteristics. Model simulations are evaluated with various data sets. Besides the well reproduction of temporal and spatial variations of aerosol components and SWDOWN in the model, AOD and SSA are used to evaluate the aerosol optical properties.

Near-surface mass concentrations of simulated BrC in the NCP range from 0.05 to ~~40.8~~42.3 μg m^{-3} with an average of ~~4.8~~5.2 μg m^{-3}, which is mainly attributed to ~~contributed by~~ RCC and BB, especially ~~evident~~ in the BTH region and Fen-Wei Plain. Estimation of the BrC contribution to AAOD shows that the BrC accounts for an average of 1~~1.2~~6.4% and up to 3~~3.6~~9.5% of the total aerosol absorption at 365 nm. The largest contributor to the

设置了格式: 突出显示

设置了格式: 突出显示

absorption of BrC is ~~the BrC from~~ RCC derived BrC, reaching 5~~5.3~~9.3%. BrC generally has a net cooling effect in the NCP if we consider both the absorption and scattering properties, with ~~its~~ DRE_{TOA} of BrC of around -0.~~10~~09 W m^{-2} on average and ~~in the~~ ranging ~~e~~ between -2.~~45~~74 W m^{-2} and +0.4~~5~~6 W m^{-2}. However, the absorption of BrC increases the DRE_{TOA} of OA by 2~~4.0~~8.0% with an average of +0.~~40~~37 W m^{-2} and ~~up~~ a maximum of~~to~~ +~~2.45~~1.83 W m^{-2}. The average ~~increased~~ increase in DRE_{TOA} of BrC from RCC, BB, secondary formation, and FFs-TRA is +0.2~~0~~6 W m^{-2}, +0.11 W m^{-2}, +0.02 W m^{-2}, +0.01 W m^{-2}, respectively. Our results indicate that BrC derived from RCC may have significant implications for regions relying heavily on coal as their primary energy source, such as northern China. Climate models should not only incorporate the absorption of BrC but also account for residential coal burning as a potentially important BrC emission source. Additionally, although we conducted simulations with a relatively conservative secondary BrC, ~~The study indicates that although the level of secondary BrC is lower than that of BrC from FFs-TRA, it causes more absorption and larger radiative effects. The pronounced radiative effect of secondary BrC may be not only attributed to their internal mixing with other water-soluble aerosols and aerosol liquid water, but also associated with the relatively low density adopted in the simulation. Although we conducted simulations with low secondary BrC,~~ the impact of secondary BrC on radiative processes should not be overlooked. More field observation and model experiments should be carried out in the future for better understanding of its role in atmospheric radiation balance.

It should be noted that China has started to switch from coal to cleaner and more efficient energy such as natural gas or liquid petroleum gas in recent years. According to the latest report of National Bureau of Statistics of China, the total coal consumption for residential use was 55.5 Gg in 2022 (https://data.stats.gov.cn) with a 40.3% decrease compared to 2014. Therefore, our diagnosis of the sources of BrC and their radiative effects is specifically targeted at the winter season in 2014. Moreover, future simulations should strengthen the parameterization for the evolution of BrC, such as bleaching or darkening processes.

The simulation of BrC in climate models is fraught with uncertainties due to its diverse sources which result in a wide range of optical properties. The absorption characteristics of BrC can change significantly as it undergoes atmospheric aging, impacting its radiative forcing estimates. Additionally, interactions of BrC with other atmospheric particles and its effects on cloud microphysics and albedo introduce further complexities in modeling its climate impact. These uncertainties necessitate enhanced observational data and better integration of BrC properties in climate models to improve the accuracy of climate predictions and assessments. Although the simulations have been evaluated with extensive aerosol mass and optical measurements, more field measurements

设置了格式: 突出显示

设置了格式: 突出显示

设置了格式: 突出显示

设置了格式: 字体: (中文) +中文正文 (等线), 10 磅, 字体颜色: 自动设置, 突出显示

带格式的: 缩进: 首行缩进: 2 字符

设置了格式: 字体: (中文) +中文正文 (等线), 10 磅, 字体颜色: 自动设置, 突出显示

设置了格式: 字体: (中文) +中文正文 (等线), 10 磅, 字体颜色: 自动设置, 突出显示

设置了格式: 字体: (中文) +中文正文 (等线), 10 磅, 字体颜色: 自动设置, 突出显示

设置了格式: 字体: (中文) +中文正文 (等线), 10 磅, 字体颜色: 自动设置, 突出显示

设置了格式: 字体: (中文) +中文正文 (等线), 10 磅, 字体颜色: 自动设置, 突出显示

设置了格式: 字体: (中文) +中文正文 (等线), 10 磅, 字体颜色: 自动设置, 突出显示

设置了格式: 字体: (中文) +中文正文 (等线), 10 磅, 字体颜色: 自动设置, 突出显示

设置了格式: 字体: (中文) +中文正文 (等线), 10 磅, 字体颜色: 自动设置

and lab experiments are needed, especially for the inventory development of BrC, the vertical profiles from aircrafts, and physicochemical properties which would be useful for further evaluating and improving model performance.

Author contributions

Guohui Li and Xuexi Tie designed the study. Jiamao Zhou and Guohui Li wrote the paper. Jiamao Zhou, Jiarui Wu, Xi Li, Ruonan Wang performed the model simulations. Xiaoli Su and Jiang Qian collected satellites and ground-based observation data. Ting Zhang, Wenting Dai and Junji Cao performed field observation and laboratory analysis. Imad El Haddad and Andre S.H. Prevot provided the data of OA components in Beijing, kindly reviewed the language writing of the manuscript and provided some supplementary suggestions for the paper. All authors reviewed and commented on the paper.

设置了格式: 突出显示

设置了格式: 突出显示

Acknowledgments

This work was financially supported by the project of Yong Scientists Fund of the National Natural Science Foundation of China (42107127).

Data availability

The Chinese Ecosystem Research Network (CERN) provided the radiation observation data. The AOD_{550} data is supported from "National Earth System Science Data Center (https://www.geodata.cn)" and AOD_{440} provided by OMI Science Team (https://www.earthdata.nasa.gov/learn/find-data/near-real-time/omi). The SSA data is supported by Sun-sky Radiometer Observation NETwork (http://www.sonet.ac.cn) and the historic profiles of the observed ambient air pollutants provided by Ministry of Ecology and Environment of China (https://www.aqistudy.cn/).

Competing interests

The authors declare that they have no conflict of interest.

References

Andreae, M. O. and Gelencsér, A.: Black carbon or brown carbon?: The nature of light-absorbing carbonaceous aerosols, Atmos. Chem. Phys., 6, 3131–3148, https://doi.org/10.5194/acp-6-3131-2006, 2006.

Bai, K., Li, K., Ma, M., Li, K., Li, Z., Guo, J., Chang, N.-B., Tan, Z., and Di Han: LGHAP: the Long-term Gap-free High-resolution Air Pollutant concentration dataset, derived via tensor-flow-based multimodal data fusion, Earth Syst. Sci. Data, 14, 907–927, https://doi.org/10.5194/essd-14-907-2022, 2022.

Bohren, C. F. and Huffman, D. R.: Absorption and Scattering of Light by Small Particles, Wiley, 1998.

Bond, T. C.: Spectral dependence of visible light absorption by carbonaceous particles emitted from coal combustion, Geophys. Res. Lett., 28, 4075–4078, https://doi.org/10.1029/2001GL013652, 2001.

Brown, H., Liu, X., Feng, Y., Jiang, Y., Wu, M., Lu, Z., Wu, C., Murphy, S., and Pokhrel, R.: Radiative effect and climate impacts of brown carbon with the Community Atmosphere Model (CAM5), Atmos. Chem. Phys., 18, 17745–17768, https://doi.org/10.5194/acp-18-17745-2018, 2018.

Browne, E. C., Zhang, X., Franklin, J. P., Ridley, K. J., Kirchstetter, T. W., Wilson, K. R., Cappa, C. D., and Kroll, J. H.: Effect of heterogeneous oxidative aging on light absorption by biomass burning organic aerosol, Aerosol Science and Technology, 53, 663–674, https://doi.org/10.1080/02786826.2019.1599321, 2019.

Cao, J. J. and Cui, L.: Current Status, Characteristics and Causes of Particulate Air Pollution in the Fenwei Plain, China: A Review, J. Geophys. Res., 126, https://doi.org/10.1029/2020JD034472, 2021.

Chakrabarty, R. K., Moosmüller, H., Chen, L.-W. A., Lewis, K., Arnott, W. P., Mazzoleni, C., Dubey, M. K., Wold, C. E., Hao, W. M., and Kreidenweis, S. M.: Brown carbon in tar balls from smoldering biomass combustion, Atmos. Chem. Phys., 10, 6363–6370, https://doi.org/10.5194/acp-10-6363-2010, 2010.

Chen, W., Wang, Z., Zhao, H., and Qin, K.: A novel way to calculate shortwave black carbon direct radiative effect, The Science of the total environment, 756, 142961, https://doi.org/10.1016/j.scitotenv.2020.142961, 2021.

Chen, Y. and Bond, T. C.: Light absorption by organic carbon from wood combustion, Atmos. Chem. Phys., 10, 1773–1787, https://doi.org/10.5194/acp-10-1773-2010, 2010.

Cheng, Z., Atwi, K. M., Yu, Z., Avery, A., Fortner, E. C., Williams, L., Majluf, F., Krechmer, J. E., Lambe, A. T., and Saleh, R.: Evolution of the light-absorption properties of combustion brown carbon aerosols following reaction with nitrate radicals, Aerosol Science and Technology, 54, 849–863, https://doi.org/10.1080/02786826.2020.1726867, 2020.

Corbin, J. C., Czech, H., Massabò, D., Mongeot, F. B. de, Jakobi, G., Liu, F., Lobo, P., Mennucci, C., Mensah, A. A., Orasche, J., Pieber, S. M., Prévôt, A. S. H., Stengel, B., Tay, L.-L., Zanatta, M., Zimmermann, R., El Haddad, I., and Gysel, M.: Infrared-absorbing carbonaceous tar can dominate light absorption by marine-engine exhaust, npj Clim Atmos Sci, 2, 3985, https://doi.org/10.1038/s41612-019-0069-5, 2019.

D'Almeida, G.A., Koepke, P. and Shettle, E.P.: Atmospheric Aerosols: Global Climatology and Radiative Characteristics, A.Deepak Publ, Hampton, Virginia, 1991.

Dubovik, O., Holben, B., Eck, T. F., Smirnov, A., Kaufman, Y. J., King, M. D., Tanré, D., and Slutsker, I.: Variability of Absorption and Optical Properties of Key Aerosol Types Observed in Worldwide Locations, J. Atmos. Sci., 59, 590–608, https://doi.org/10.1175/1520-0469(2002)059<0590:VOAAOP>2.0.CO;2, 2002.

Fast, J. D., Gustafson, W. I., Easter, R. C., Zaveri, R. A., Barnard, J. C., Chapman, E. G., Grell, G. A., and Peckham, S. E.: Evolution of ozone, particulates, and aerosol direct radiative forcing in the vicinity of Houston using a fully coupled meteorology-chemistry-aerosol model, J. Geophys. Res., 111, 2981,

https://doi.org/10.1029/2005JD006721, 2006.
Feng, Y., Ramanathan, V., and Kotamarthi, V. R.: Brown carbon: A significant atmospheric absorber of solar radiation?, Atmos. Chem. Phys., 13, 8607–8621, 2013.
Forrister, H., Liu, J., Scheuer, E., Dibb, J., Ziemba, L., Thornhill, K. L., Anderson, B., Diskin, G., Perring, A. E., Schwarz, J. P., Campuzano-Jost, P., Day, D. A., Palm, B. B., Jimenez, J. L., Nenes, A., and Weber, R. J.: Evolution of brown carbon in wildfire plumes, Geophys. Res. Lett., 42, 4623–4630, https://doi.org/10.1002/2015GL063897, 2015.
Fountoukis, C. and Nenes, A.: ISORROPIA II: a computationally efficient thermodynamic equilibrium model for K^+–Ca^{2+}–Mg^{2+}–NH_4^+–Na^+–SO_4^{2-}–NO_3^-–Cl^-–H_2O aerosols, Atmos. Chem. Phys., 7, 4639–4659, https://doi.org/10.5194/acp-7-4639-2007, 2007.
Gao, Y., Gao, P., Zhuang, B., Hu, Y., Zhou, Y., Wang, T., Li, S., Li, M., and Xie, M.: Changes in the Climate Effects of Major Anthropogenic Aerosols in East Asia Under Different Emission Reduction Scenarios in China, J. Geophys. Res., 130, https://doi.org/10.1029/2024JD042301, 2025.
Ge, W., Prime, N. S., Smith, S. J., Liu, J., Ren, Y., Zhou, Y., Wu, H., Wang, X., and Chen, G.: The short-term comprehensive impact of the phase-out of global coal combustion on air pollution and climate change, Environmental pollution (Barking, Essex 1987), 367, 125669, https://doi.org/10.1016/j.envpol.2025.125669, 2025.
Gouw, J. A. de, Middlebrook, A. M., Warneke, C., Goldan, P. D., Kuster, W. C., Roberts, J. M., Fehsenfeld, F. C., Worsnop, D. R., Canagaratna, M. R., Pszenny, A. A. P., Keene, W. C., Marchewka, M., Bertman, S. B., and Bates, T. S.: Budget of organic carbon in a polluted atmosphere: Results from the New England Air Quality Study in 2002, J. Geophys. Res., 110, https://doi.org/10.1029/2004JD005623, 2005.
Grell, G. A., Peckham, S. E., Schmitz, R., McKeen, S. A., Frost, G., Skamarock, W. C., and Eder, B.: Fully coupled "online" chemistry within the WRF model, Atmospheric Environment, 39, 6957–6975, https://doi.org/10.1016/j.atmosenv.2005.04.027, 2005.
Guenther, A., Karl, T., Harley, P., Wiedinmyer, C., Palmer, P. I., and Geron, C.: Estimates of global terrestrial isoprene emissions using MEGAN (Model of Emissions of Gases and Aerosols from Nature), Atmos. Chem. Phys., 6, 3181–3210, https://doi.org/10.5194/acp-6-3181-2006, 2006.
Hammer, M. S., Martin, R. V., van Donkelaar, A., Buchard, V., Torres, O., Ridley, D. A., and Spurr, R. J. D.: Interpreting the ultraviolet aerosol index observed with the OMI satellite instrument to understand absorption by organic aerosols: Implications for atmospheric oxidation and direct radiative effects, Atmos. Chem. Phys., 16, 2507–2523, https://doi.org/10.5194/acp-16-2507-2016, 2016.
Hoffer, A., Gelencsér, A., Guyon, P., Kiss, G., Schmid, O., Frank, G. P., Artaxo, P., and Andreae, M. O.: Optical properties of humic-like substances (HULIS) in biomass-burning aerosols, Atmos. Chem. Phys., 6, 3563–3570, https://doi.org/10.5194/acp-6-3563-2006, 2006.
Huang, R.-j., Yuan, W., Yang, L., Yang, H., Cao, W., Guo, J., Zhang, N., Zhu, C., Wu, Y., and Zhang, R.: Concentration, optical characteristics, and emission factors of brown carbon emitted by on-road vehicles, The Science of the total environment, 810, 151307, https://doi.org/10.1016/j.scitotenv.2021.151307, 2022.
Huang, X., Song, Y., Zhao, C., Cai, X., Zhang, H., and Zhu, T.: Direct Radiative Effect by Multicomponent Aerosol over China*, Journal of Climate, 28, 3472–3495, https://doi.org/10.1175/JCLI-D-14-00365.1, 2015.
Hurley, M. D., Sokolov, O., Wallington, T. J., Takekawa, H., Karasawa, M., Klotz, B., Barnes, I., and Becker, K.

H.: Organic aerosol formation during the atmospheric degradation of toluene, Environmental science & technology, 35, 1358–1366, https://doi.org/10.1021/es0013733, 2001.

IPCC (Ed.): Climate Change 2013: The Physical Science Basis. Contribution of Working Group I to the Fifth Assessment Report of the Intergovernmental Panel on Climate Change, Cambridge University Press, Cambridge, United Kingdom and New York, NY, USA, 2013.

Jacobson, M. Z.: Effects of biomass burning on climate, accounting for heat and moisture fluxes, black and brown carbon, and cloud absorption effects, J. Geophys. Res., 119, 8980–9002, https://doi.org/10.1002/2014JD021861, 2014.

Jacobson, M. Z.: Isolating nitrated and aromatic aerosols and nitrated aromatic gases as sources of ultraviolet light absorption, J. Geophys. Res., 104, 3527–3542, https://doi.org/10.1029/1998JD100054, 1999.

Jeong, J. I., Jo, D. S., Park, R. J., Lee, H.-M., Curci, G., and Kim, S.-W.: Parametric analysis for global single scattering albedo calculations, Atmospheric Environment, 234, 117616, https://doi.org/10.1016/j.atmosenv.2020.117616, 2020.

Jo, D. S., Nault, B. A., Tilmes, S., Gettelman, A., McCluskey, C. S., Hodzic, A., Henze, D. K., Nawaz, M. O., Fung, K. M., and Jimenez, J. L.: Global Health and Climate Effects of Organic Aerosols from Different Sources, Environmental science & technology, 57, 13793–13807, https://doi.org/10.1021/acs.est.3c02823, 2023.

Jo, D. S., Park, R. J., Lee, S., Kim, S.-W., and Zhang, X.: A global simulation of brown carbon: Implications for photochemistry and direct radiative effect, Atmos. Chem. Phys., 16, 3413–3432, https://doi.org/10.5194/acp-16-3413-2016, 2016.

Kawamura, K., Imai, Y., and Barrie, L. A.: Photochemical production and loss of organic acids in high Arctic aerosols during long-range transport and polar sunrise ozone depletion events, Atmospheric Environment, 39, 599–614, https://doi.org/10.1016/j.atmosenv.2004.10.020, 2005.

Kirchstetter, T. W., Novakov, T., and Hobbs, P. V.: Evidence that the spectral dependence of light absorption by aerosols is affected by organic carbon, J. Geophys. Res., 109, n/a-n/a, https://doi.org/10.1029/2004JD004999, 2004.

Kumar, N. K., Corbin, J. C., Bruns, E. A., Massabó, D., Slowik, J. G., Drinovec, L., Močnik, G., Prati, P., Vlachou, A., Baltensperger, U., Gysel, M., El-Haddad, I., and Prévôt, A. S. H.: Production of particulate brown carbon during atmospheric aging of residential wood-burning emissions, Atmos. Chem. Phys., 18, 17843–17861, https://doi.org/10.5194/acp-18-17843-2018, 2018.

Lack, D. A., Langridge, J. M., Bahreini, R., Cappa, C. D., Middlebrook, A. M., and Schwarz, J. P.: Brown carbon and internal mixing in biomass burning particles, Proceedings of the National Academy of Sciences of the United States of America, 109, 14802–14807, https://doi.org/10.1073/pnas.1206575109, 2012.

Laskin, A., Laskin, J., and Nizkorodov, S. A.: Chemistry of atmospheric brown carbon, Chemical reviews, 115, 4335–4382, https://doi.org/10.1021/cr5006167, 2015.

Li, C., He, Q., Hettiyadura, A. P. S., Käfer, U., Shmul, G., Meidan, D., Zimmermann, R., Brown, S. S., George, C., Laskin, A., and Rudich, Y.: Formation of Secondary Brown Carbon in Biomass Burning Aerosol Proxies through NO3 Radical Reactions, Environmental science & technology, 54, 1395–1405, https://doi.org/10.1021/acs.est.9b05641, 2020.

Li, G., Lei, W., Bei, N., and Molina, L. T.: Contribution of garbage burning to chloride and $PM_{2.5}$ in Mexico City, Atmos. Chem. Phys., 12, 8751–8761, https://doi.org/10.5194/acp-12-8751-2012, 2012.

Li, G., Bei, N., Tie, X., and Molina, L. T.: Aerosol effects on the photochemistry in Mexico City during MCMA-2006/MILAGRO campaign, Atmos. Chem. Phys., 11, 5169–5182, https://doi.org/10.5194/acp-11-5169-2011, 2011a.

Li, G., Zavala, M., Lei, W., Tsimpidi, A. P., Karydis, V. A., Pandis, S. N., Canagaratna, M. R., and Molina, L. T.: Simulations of organic aerosol concentrations in Mexico City using the WRF-CHEM model during the MCMA-2006/MILAGRO campaign, Atmos. Chem. Phys., 11, 3789–3809, https://doi.org/10.5194/acp-11-3789-2011, 2011b.

Li, G., Lei, W., Zavala, M., Volkamer, R., Dusanter, S., Stevens, P., and Molina, L. T.: Impacts of HONO sources on the photochemistry in Mexico City during the MCMA-2006/MILAGO Campaign, Atmos. Chem. Phys., 10, 6551–6567, https://doi.org/10.5194/acp-10-6551-2010, 2010.

Li, M., Fan, X., Zhu, M., Zou, C., Song, J., Wei, S., Jia, W., and Peng, P.'a.: Abundance and Light Absorption Properties of Brown Carbon Emitted from Residential Coal Combustion in China, Environmental science & technology, 53, 595–603, https://doi.org/10.1021/acs.est.8b05630, 2019.

Li, M., Liu, H., Geng, G., Hong, C., Liu, F., Song, Y., Tong, D., Zheng, B., Cui, H., Man, H., Zhang, Q., and He, K.: Anthropogenic emission inventories in China: a review, National Science Review, 4, 834–866, https://doi.org/10.1093/nsr/nwx150, 2017.

Li, X., Wu, J., Elser, M., Feng, T., Cao, J., El-Haddad, I., Huang, R., Tie, X., Prévôt, A. S. H., and Li, G.: Contributions of residential coal combustion to the air quality in Beijing–Tianjin–Hebei (BTH), China: a case study, Atmos. Chem. Phys., 18, 10675–10691, https://doi.org/10.5194/acp-18-10675-2018, 2018.

Lin, G., Penner, J. E., Flanner, M. G., Sillman, S., Xu, L., and Zhou, C.: Radiative forcing of organic aerosol in the atmosphere and on snow: Effects of SOA and brown carbon, J. Geophys. Res., 119, 7453–7476, https://doi.org/10.1002/2013JD021186, 2014.

Lin, P., Bluvshtein, N., Rudich, Y., Nizkorodov, S. A., Laskin, J., and Laskin, A.: Molecular Chemistry of Atmospheric Brown Carbon Inferred from a Nationwide Biomass Burning Event, Environmental science & technology, 51, 11561–11570, https://doi.org/10.1021/acs.est.7b02276, 2017.

Liu, D., Whitehead, J., Alfarra, M. R., Reyes-Villegas, E., Spracklen, D. V., Reddington, C. L., Kong, S., Williams, P. I., Ting, Y.-C., Haslett, S., Taylor, J. W., Flynn, M. J., Morgan, W. T., McFiggans, G., Coe, H., and Allan, J. D.: Black-carbon absorption enhancement in the atmosphere determined by particle mixing state, Nature Geosci, 10, 184–188, https://doi.org/10.1038/ngeo2901, 2017.

Liu, J., Bergin, M., Guo, H., King, L., Kotra, N., Edgerton, E., and Weber, R. J.: Size-resolved measurements of brown carbon in water and methanol extracts and estimates of their contribution to ambient fine-particle light absorption, Atmos. Chem. Phys., 13, 12389–12404, https://doi.org/10.5194/acp-13-12389-2013, 2013.

Lu, Z., Streets, D. G., Winijkul, E., Yan, F., Chen, Y., Bond, T. C., Feng, Y., Dubey, M. K., Liu, S., Pinto, J. P., and Carmichael, G. R.: Light absorption properties and radiative effects of primary organic aerosol emissions, Environmental science & technology, 49, 4868–4877, https://doi.org/10.1021/acs.est.5b00211, 2015.

Ma, Y., Jin, Y., Zhang, M., Gong, W., Hong, J., Jin, S., Shi, Y., Zhang, Y., and Liu, B.: Aerosol optical properties of haze episodes in eastern China based on remote-sensing observations and WRF-Chem simulations, The Science of the total environment, 757, 143784, https://doi.org/10.1016/j.scitotenv.2020.143784, 2021.

Maria, S. F., Russell, L. M., Turpin, B. J., Porcja, R. J., Campos, T. L., Weber, R. J., and Huebert, B. J.: Source signatures of carbon monoxide and organic functional groups in Asian Pacific Regional Aerosol Characterization

689 Experiment (ACE-Asia) submicron aerosol types, J. Geophys. Res., 108, 295,
690 https://doi.org/10.1029/2003JD003703, 2003.
691 Mo, Y., Li, J., Cheng, Z., Zhong, G., Zhu, S., Tian, C., Chen, Y., and Zhang, G.: Dual Carbon Isotope-Based
692 Source Apportionment and Light Absorption Properties of Water-Soluble Organic Carbon in PM 2.5 Over China,
693 J. Geophys. Res., 126, 27805, https://doi.org/10.1029/2020JD033920, 2021.
694 Moise, T., Flores, J. M., and Rudich, Y.: Optical properties of secondary organic aerosols and their changes by
695 chemical processes, Chemical reviews, 115, 4400–4439, https://doi.org/10.1021/cr5005259, 2015.
696 Mukai, H. and Ambe, Y.: Characterization of a humic acid-like brown substance in airborne particulate matter and
697 tentative identification of its origin, Atmospheric Environment (1967), 20, 813–819, https://doi.org/10.1016/0004-
698 6981(86)90265-9, 1986.
699 Nenes, A., Pandis, S. N., and Pilinis Christodoulos: ISORROPIA: A New Thermodynamic Equilibrium Model for
700 Multiphase Multicomponent Inorganic Aerosols, Aquatic Geochemistry, 4, 123–152, 1998.
701 Ni, H., Huang, R.-j., Pieber, S. M., Corbin, J. C., Stefenelli, G., Pospisilova, V., Klein, F., Gysel-Beer, M., Yang,
702 L., Baltensperger, U., Haddad, I. E., Slowik, J. G., Cao, J., Prévôt, A. S. H., and Dusek, U.: Brown Carbon in
703 Primary and Aged Coal Combustion Emission, Environmental science & technology, 55, 5701–5710,
704 https://doi.org/10.1021/acs.est.0c08084, 2021.
705 Park, R. J., Kim, M. J., Jeong, J. I., Youn, D., and Kim, S.: A contribution of brown carbon aerosol to the aerosol
706 light absorption and its radiative forcing in East Asia, Atmospheric Environment, 44, 1414–1421,
707 https://doi.org/10.1016/j.atmosenv.2010.01.042, 2010.
708 Peng, C., Razafindrambinina, P. N., Malek, K. A., Chen, L., Wang, W., Huang, R.-j., Zhang, Y., Ding, X., Ge, M.,
709 Wang, X., Asa-Awuku, A. A., and Tang, M.: Interactions of organosulfates with water vapor under sub- and
710 supersaturated conditions, Atmos. Chem. Phys., 21, 7135–7148, https://doi.org/10.5194/acp-21-7135-2021, 2021.
711 Pokhrel, R. P., Beamesderfer, E. R., Wagner, N. L., Langridge, J. M., Lack, D. A., Jayarathne, T., Stone, E. A.,
712 Stockwell, C. E., Yokelson, R. J., and Murphy, S. M.: Relative importance of black carbon, brown carbon, and
713 absorption enhancement from clear coatings in biomass burning emissions, Atmos. Chem. Phys., 17, 5063–5078,
714 https://doi.org/10.5194/acp-17-5063-2017, 2017.
715 Saleh, R.: From Measurements to Models: Toward Accurate Representation of Brown Carbon in Climate
716 Calculations, Curr Pollution Rep, 6, 90–104, https://doi.org/10.1007/s40726-020-00139-3, 2020.
717 Saleh, R., Cheng, Z., and Atwi, K.: The Brown–Black Continuum of Light-Absorbing Combustion Aerosols,
718 Environ. Sci. Technol. Lett., 5, 508–513, https://doi.org/10.1021/acs.estlett.8b00305, 2018.
719 Saleh, R., Robinson, E. S., Tkacik, D. S., Ahern, A. T., Liu, S., Aiken, A. C., Sullivan, R. C., Presto, A. A., Dubey,
720 M. K., Yokelson, R. J., Donahue, N. M., and Robinson, A. L.: Brownness of organics in aerosols from biomass
721 burning linked to their black carbon content, Nature Geosci, 7, 647–650, https://doi.org/10.1038/ngeo2220, 2014.
722 Song, S., Wang, Y., Wang, Y., Wang, T., and Tan, H.: The characteristics of particulate matter and optical properties
723 of Brown carbon in air lean condition related to residential coal combustion, Powder Technology, 379, 505–514,
724 https://doi.org/10.1016/j.powtec.2020.10.082, 2021.
725 Stokes, R. H. and Robinson, R. A.: Interactions in Aqueous Nonelectrolyte Solutions. I. Solute-Solvent Equilibria,
726 J. Phys. Chem., 70, 2126–2131, https://doi.org/10.1021/j100879a010, 1966.
727 Sun, J., Zhang, Y., Zhi, G., Hitzenberger, R., Jin, W., Chen, Y., Wang, L., Tian, C., Li, Z., Chen, R., Xiao, W.,
728 Cheng, Y., Yang, W., Yao, L., Cao, Y., Huang, D., Qiu, Y., Xu, J., Xia, X., Yang, X., Zhang, X., Zong, Z., Song,

729 Y., and Wu, C.: Brown carbon's emission factors and optical characteristics in household biomass burning:
730 Developing a novel algorithm for estimating the contribution of brown carbon, Atmos. Chem. Phys., 21, 2329–
731 2341, https://doi.org/10.5194/acp-21-2329-2021, 2021.
732 Sun, J., Zhi, G., Hitzenberger, R., Chen, Y., Tian, C., Zhang, Y., Feng, Y., Cheng, M., Zhang, Y., Cai, J., Chen, F.,
733 Qiu, Y., Jiang, Z., Li, J., Zhang, G., and Mo, Y.: Emission factors and light absorption properties of brown carbon
734 from household coal combustion in China, Atmos. Chem. Phys., 17, 4769–4780, https://doi.org/10.5194/acp-17-
735 4769-2017, 2017.
736 Tang, J., Li, J., Su, T., Han, Y., Mo, Y., Jiang, H., Cui, M., Jiang, B., Chen, Y., Tang, J., Song, J., Peng, P.'a., and
737 Zhang, G.: Molecular compositions and optical properties of dissolved brown carbon in biomass burning, coal
738 combustion, and vehicle emission aerosols illuminated by excitation–emission matrix spectroscopy and Fourier
739 transform ion cyclotron resonance mass spectrometry analysis, Atmos. Chem. Phys., 20, 2513–2532,
740 https://doi.org/10.5194/acp-20-2513-2020, 2020.
741 Tian, J., Wang, Q., Ni, H., Wang, M., Zhou, Y., Han, Y., Shen, Z., Pongpiachan, S., Zhang, N., Zhao, Z., Zhang,
742 Q., Zhang, Y., Long, X., and Cao, J.: Emission Characteristics of Primary Brown Carbon Absorption From
743 Biomass and Coal Burning: Development of an Optical Emission Inventory for China, J. Geophys. Res. Atmos.,
744 15, 27,805, https://doi.org/10.1029/2018JD029352, 2019.
745 Tsigaridis, K. and Kanakidou, M.: The Present and Future of Secondary Organic Aerosol Direct Forcing on
746 Climate, Curr Clim Change Rep, 4, 84–98, https://doi.org/10.1007/s40641-018-0092-3, 2018.
747 Tuccella, P., Curci, G., Pitari, G., Lee, S., and Jo, D. S.: Direct Radiative Effect of Absorbing Aerosols: Sensitivity
748 to Mixing State, Brown Carbon, and Soil Dust Refractive Index and Shape, J. Geophys. Res. Atmos., 125, 317,
749 https://doi.org/10.1029/2019JD030967, 2020.
750 Turpin, B. J. and Lim, H.-J.: Species Contributions to PM2.5 Mass Concentrations: Revisiting Common
751 Assumptions for Estimating Organic Mass, Aerosol Science and Technology, 35, 602–610,
752 https://doi.org/10.1080/02786820152051454, 2001.
753 Wang, J., Ye, J., Zhang, Q., Zhao, J., Wu, Y., Li, J., Liu, D., Li, W., Zhang, Y., Wu, C., Xie, C., Qin, Y., Lei, Y.,
754 Huang, X., Guo, J., Liu, P., Fu, P., Li, Y., Lee, H. C., Choi, H., Zhang, J., Liao, H., Chen, M., Sun, Y., Ge, X.,
755 Martin, S. T., and Jacob, D. J.: Aqueous production of secondary organic aerosol from fossil-fuel emissions in
756 winter Beijing haze, Proceedings of the National Academy of Sciences of the United States of America, 118,
757 https://doi.org/10.1073/pnas.2022179118, 2021.
758 Wang, Q., Zhou, Y., Ma, N., Zhu, Y., Zhao, X., Zhu, S., Tao, J., Hong, J., Wu, W., Cheng, Y., and Su, H.: Review
759 of Brown Carbon Aerosols in China: Pollution Level, Optical Properties, and Emissions, J. Geophys. Res., 127,
760 455, 2022a.
761 Wang, Q., Wang, L., Gong, C., Li, M., Xin, J., Tang, G., Sun, Y., Gao, J., Wang, Y., Wu, S., Kang, Y., Yang, Y., Li,
762 T., Liu, J., and Wang, Y.: Vertical evolution of black and brown carbon during pollution events over North China
763 Plain, The Science of the total environment, 806, 150950, https://doi.org/10.1016/j.scitotenv.2021.150950, 2022b.
764 Wang, X., Heald, C. L., Ridley, D. A., Schwarz, J. P., Spackman, J. R., Perring, A. E., Coe, H., Liu, D., and Clarke,
765 A. D.: Exploiting simultaneous observational constraints on mass and absorption to estimate the global direct
766 radiative forcing of black carbon and brown carbon, Atmos. Chem. Phys., 14, 10989–11010,
767 https://doi.org/10.5194/acp-14-10989-2014, 2014.
768 Wang, X., Heald, C. L., Liu, J., Weber, R. J., Campuzano-Jost, P., Jimenez, J. L., Schwarz, J. P., and Perring, A.

E.: Exploring the observational constraints on the simulation of brown carbon, Atmos. Chem. Phys., 18, 635–653, https://doi.org/10.5194/acp-18-635-2018, 2018.

Wang, Y., Wang, Y., Song, S., Wang, T., Li, D., and Tan, H.: Effects of coal types and combustion conditions on carbonaceous aerosols in flue gas and their light absorption properties, Fuel, 277, 118148, https://doi.org/10.1016/j.fuel.2020.118148, 2020.

Washenfelder, R. A., Attwood, A. R., Brock, C. A., Guo, H., Xu, L., Weber, R. J., Ng, N. L., Allen, H. M., Ayres, B. R., Baumann, K., Cohen, R. C., Draper, D. C., Duffey, K. C., Edgerton, E., Fry, J. L., Hu, W. W., Jimenez, J. L., Palm, B. B., Romer, P., Stone, E. A., Wooldridge, P. J., and Brown, S. S.: Biomass burning dominates brown carbon absorption in the rural southeastern United States, Geophys. Res. Lett., 42, 653–664, https://doi.org/10.1002/2014GL062444, 2015.

Wong, J. P. S., Tsagkaraki, M., Tsiodra, I., Mihalopoulos, N., Violaki, K., Kanakidou, M., Sciare, J., Nenes, A., and Weber, R. J.: Atmospheric evolution of molecular-weight-separated brown carbon from biomass burning, Atmos. Chem. Phys., 19, 7319–7334, https://doi.org/10.5194/acp-19-7319-2019, 2019.

Wu, J., Bei, N., Hu, B., Liu, S., Wang, Y., Shen, Z., Li, X., Liu, L., Wang, R., Liu, Z., Cao, J., Tie, X., Molina, L. T., and Li, G.: Aerosol-photolysis interaction reduces particulate matter during wintertime haze events, Proceedings of the National Academy of Sciences of the United States of America, 117, 9755–9761, https://doi.org/10.1073/pnas.1916775117, 2020.

Xie, C., Xu, W., Wang, J., Wang, Q., Liu, D., Tang, G., Chen, P., Du, W., Zhao, J., Zhang, Y., Zhou, W., Han, T., Bian, Q., Li, J., Fu, P., Wang, Z., Ge, X., Allan, J., Coe, H., and Sun, Y.: Vertical characterization of aerosol optical properties and brown carbon in winter in urban Beijing, China, Atmos. Chem. Phys., 19, 165–179, https://doi.org/10.5194/acp-19-165-2019, 2019.

Xie, M., Hays, M. D., and Holder, A. L.: Light-absorbing organic carbon from prescribed and laboratory biomass burning and gasoline vehicle emissions, Scientific reports, 7, 7318, https://doi.org/10.1038/s41598-017-06981-8, 2017.

Xu, L., Lin, G., Liu, X., Wu, C., Wu, Y., and Lou, S.: Constraining Light Absorption of Brown Carbon in China and Implications for Aerosol Direct Radiative Effect, Geophys. Res. Lett., 51, 455, https://doi.org/10.1029/2024GL109861, 2024.

Yan, C., Zheng, M., Bosch, C., Andersson, A., Desyaterik, Y., Sullivan, A. P., Collett, J. L., Zhao, B., Wang, S., He, K., and Gustafsson, Ö.: Important fossil source contribution to brown carbon in Beijing during winter, Scientific reports, 7, 43182, https://doi.org/10.1038/srep43182, 2017.

Yan, J., Wang, X., Gong, P., Wang, C., and Cong, Z.: Review of brown carbon aerosols: Recent progress and perspectives, The Science of the total environment, 634, 1475–1485, https://doi.org/10.1016/j.scitotenv.2018.04.083, 2018.

Yang, M., Howell, S. G., Zhuang, J., and Huebert, B. J.: Attribution of aerosol light absorption to black carbon, brown carbon, and dust in China – interpretations of atmospheric measurements during EAST-AIRE, Atmos. Chem. Phys., 9, 2035–2050, https://doi.org/10.5194/acp-9-2035-2009, 2009.

Zhang, A., Wang, Y., Zhang, Y., Weber, R. J., Song, Y., Ke, Z., and Zou, Y.: Modeling the global radiative effect of brown carbon: A potentially larger heating source in the tropical free troposphere than black carbon, Atmos. Chem. Phys., 20, 1901–1920, https://doi.org/10.5194/acp-20-1901-2020, 2020.

Zhang, Q., Streets, D. G., Carmichael, G. R., He, K. B., Huo, H., Kannari, A., Klimont, Z., Park, I. S., Reddy, S.,

Fu, J. S., Chen, D., Duan, L., Lei, Y., Wang, L. T., and Yao, Z. L.: Asian emissions in 2006 for the NASA INTEX-B mission, Atmos. Chem. Phys., 9, 5131–5153, https://doi.org/10.5194/acp-9-5131-2009, 2009.

Zhang, Q., Li, Z., Shen, Z., Zhang, T., Zhang, Y., Sun, J., Zeng, Y., Xu, H., Wang, Q., Hang Ho, S. S., and Cao, J.: Source profiles of molecular structure and light absorption of PM2.5 brown carbon from residential coal combustion emission in Northwestern China, Environmental pollution (Barking, Essex 1987), 299, 118866, https://doi.org/10.1016/j.envpol.2022.118866, 2022a.

Zhang, W., Wang, W., Li, J., Ma, S., Lian, C., Li, K., Shi, B., Liu, M., Li, Y., Wang, Q., Sun, Y., Tong, S., and Ge, M.: Light absorption properties and potential sources of brown carbon in Fenwei Plain during winter 2018-2019, Journal of environmental sciences (China), 102, 53–63, https://doi.org/10.1016/j.jes.2020.09.007, 2021.

Zhang, Y., Wang, Q., Tian, J., Li, Y., Liu, H., Ran, W., Han, Y., Prévôt, A. S.H., and Cao, J.: Impact of COVID-19 lockdown on the optical properties and radiative effects of urban brown carbon aerosol, Geoscience Frontiers, 13, 101320, https://doi.org/10.1016/j.gsf.2021.101320, 2022b.

Zhao, C., Ruby Leung, L., Easter, R., Hand, J., and Avise, J.: Characterization of speciated aerosol direct radiative forcing over California, J. Geophys. Res., 118, 2372–2388, https://doi.org/10.1029/2012JD018364, 2013.

Zhu, Y., Wang, Q., Yang, X., Yang, N., and Wang, X.: Modeling Investigation of Brown Carbon Aerosol and Its Light Absorption in China, Atmosphere, 12, 892, https://doi.org/10.3390/atmos12070892, 2021.

S1 WRF-Chem model general description and configuration

In this study, a specific version of the WRF-Chem model (Grell et al., 2005) with modified by Li et al. (2010; 2011a; 2011b; 2012) is used to quantitatively estimate the radiative effect of brown carbon in the NCP. The model was run at a horizontal resolution of 6km with 35 vertical levels, and configured with a single domain (no nesting) of 300×300 grid cells centered at grid point at latitude of 38.0 N and longitude of 116.0 W as shown in Table S1. The model contains a new flexible gas phase chemical module which utilized with SAPRC chemistry mechanism based on the available emission inventory in the present study. The gas-phase chemistry is solved by an Eulerian backward Gauss-Seidel iterative technique with a number of iterations, inherited from NCAR-HANK (Hess et al., 2000).

For the aerosol simulations, the CMAQ/models3 aerosol module (AERO5) developed by US EPA has incorporated into the model (Binkowski and Roselle, 2003). The particle size distribution is represented as the superposition of three lognormal modes. The processes of coagulation, particles growth by the addition of mass, and new particle formation are included. The wet deposition follows the method in the CMAQ module and the dry deposition of chemical species is parameterized following Wesely (1989). The photolysis rates are calculated using the Fast Tropospheric Ultraviolet and Visible (FTUV) Radiation Model ((Tie, 2003; Li et al., 2005) , with the aerosol and cloud effects on the photochemistry (Li et al., 2011a). The inorganic aerosols is predicted with ISORROPIA (version 1.7) (Nenes et al., 1998) which calculates the thermodynamic equilibrium between the ammonia-sulfate-nitrate-chloride-water aerosols and their gas phase precursors of H_2SO_4-HNO_3-NH_3-HCl-water vapor.

The organic aerosol (OA) module is based on the volatility basis-set (VBS) approach with aging (Li et al., 2011b). The primary organic aerosol (POA) are assumed semi-volatile and photochemically reactive (Robinson et al., 2007) and distributed in logarithmically spaced volatility bins. Nine surrogate species are used for POA components followed by Shrivastava et al. (2008) with saturation concentrations (C*) ranging from 10^{-2} to 10^{6} μg m^{-3} at room temperature. The secondary organic aerosol (SOA) formation from each anthropogenic or biogenic precursor is calculated using four semi-volatile VOCs with effective saturation concentrations of 1, 10, 100, and 1000 μg m^{-3} at 298 K. The SOA formation via the heterogeneous reaction of glyoxal and methylglyoxal is parameterized as a first-order irreversible uptake by aerosol particles with an uptake coefficient of 3.7×10^{-3} (Liggio, 2005; Zhao et al.,

2006; Volkamer et al., 2007). The OA module has reasonably reproduced the POA and SOA concentration against measurements, and detailed model performance can be found in Li et al. (2011b), Feng et al. (2016), and Xing et al. (2019).

Table S1 WRF-Chem model configurations.

Parameter	Configuration
Regions	The North China Plain (NCP)
Simulation period	January 1 to 30, 2014
Domain size	300 × 300
Domain center	38.0°N, 116.0°E
Horizontal resolution	6km × 6km
Vertical resolution	35 vertical levels with a stretched vertical grid with spacing ranging from 30m near the surface, to 500m at 2.5km and 1km above 14km
Microphysics scheme	WSM 6-class graupel scheme (Hong and Lim, 2006)
Boundary layer scheme	MYJ TKE scheme (Janjić, 2002)
Surface layer scheme	MYJ surface scheme (Janjić, 2002)
Land-surface scheme	Unified Noah land-surface model (Chen and Dudhia, 2001)
Long-wave radiation scheme	Goddard longwave scheme (Chou et al., 2001)
Short-wave radiation scheme	Goddard shortwave scheme (Chou and Suarez, 1999)
Meteorological boundary and initial conditions	NCEP 1°×1° reanalysis data
Chemical initial and boundary conditions	MOZART 6-hour output (Horowitz et al., 2003)
Anthropogenic emission inventory	SAPRC-99 chemical mechanism emissions developed by Zhang et al. (2009)and Li et al.(2017)
Biogenic emission inventory	MEGAN model developed by Guenther et al. (2006)
Four-dimension data assimilation	NCEP ADP Global Air Observational Weather Data
Model spin-up time	24 hours

S2 Data and methodology

S2.1 Observation data description

The hourly near-surface measurements of O_3, NO_2, SO_2, CO and $PM_{2.5}$ concentrations have been released in public by the Ministry of Ecology and Environment of China since 2013. The submicron sulfate, nitrate, ammonium, elemental carbon and organic aerosols obtained in two cities including Beijing, Tianjin and the hourly observation of primary OA from, BB, RCC and motor vehicles emissions and SOA in Beijing in January, 2014 are provided by Institute of Earth Environment, Chinese Academy of Sciences. The organic carbon and elemental carbon concentrations are measured using a thermal/optical reflectance carbon analyzer (Model 2001, DRI, USA) (Chow et al., 2004) and water-soluble ions are measured using a DX600 ion chromatograph (Dionex Inc., Sunnyvale, CA, USA)

(Zhang et al., 2011). The SWDOWN is measured by CM-11 pyranometers at five sites from Chinese Ecosystem Research Network (CERN) in the NCP, including Beijing, Tianjin, Zhengzhou, Hefei, and Ji'nan. The hourly measurement of OA in Beijing is measured by the Aerodyne high-resolution time-of-flight aerosol mass spectrometer (HR-ToF-AMS) with a $PM_{2.5}$ lens from 9 to 25 January, 2014 at the Institute of Remote Sensing and Digital Earth, Chinese Academy of Sciences (Li et al., 2018). The positive matrix factorization (PMF) method is used to distinguish the sources of OA as hydrocarbon-like OA, biomass burning OA, coal combustion OA (Elser et al., 2016), which are interpreted for surrogates of primary OA (POA)-TRA, POA-BB, POA-COAL, and oxygenated OA is the surrogate of SOA in this paper.

S2.2 Statistical metrics for simulation comparisons

In this study, the mean bias (MB), root mean square error (RMSE) and the index of agreement (IOA) are used to evaluate the model performance in simulating air pollutants.

$$\mathrm{MB} = \frac{1}{\mathrm{N}}\sum_{\mathrm{i}=1}^{\mathrm{N}}(\mathrm{P_i} - \mathrm{O_i}) \quad (1)$$

$$\mathrm{RMSE} = \left[\frac{1}{\mathrm{N}}\sum_{\mathrm{i}=1}^{\mathrm{N}}(\mathrm{P_i} - \mathrm{O_i})^2\right]^{\frac{1}{2}} \quad (2)$$

$$\mathrm{IOA} = 1 - \frac{\sum_{\mathrm{i}=1}^{\mathrm{N}}(\mathrm{P_i}-\mathrm{O_i})^2}{\sum_{\mathrm{i}=1}^{\mathrm{N}}(|\mathrm{P_i}-\bar{\mathrm{O}}|+|\mathrm{O_i}-\bar{\mathrm{O}}|)^2} \quad (3)$$

Where P_i and O_i are the simulated and observed variables, respectively. N is the total number of the simulations for comparisons, and $\bar{O}$ donates the average of the observations. The IOA ranges from 0 to 1, with 1 showing a perfect agreement of the simulations with the observations.

S3 Model performance

S3.1 Air pollutants simulations in the NCP

Comparison of observed (black dots) and simulated (solid dark blue lines) near-surface hourly mass concentrations of (a) $PM_{2.5}$, (b) O_3, (c) NO_2, (d) SO_2, and (d) CO averaged at available monitoring sites in the NCP from January 1 to January 30, 2014 is shown in Fig. S1. The model successfully reproduces the diurnal variation of near-surface $PM_{2.5}$ concentrations in the NCP with an IOA of 0.92 and a slightly overestimation with a MB of 3.8 μg m^{-3}. The model generally captures well the temporal variations of near-surface O_3 concentrations compared to observations in the NCP with an IOA of 0.90 while a generally overestimates the O_3 concentrations a MB of 0.6 μg m^{-3}. The model also reasonably well yields

the temporal variation of NO_2, SO_2 and CO compared with observation, with IOA and MB of 0.82 and -4.0 μg m^{-3}, 0.72 and -13.2 μg m^{-3}, 0.85 and 0.0 μg m^{-3}, respectively.

The spatial pattern of calculated and observed average near-surface concentrations of $PM_{2.5}$, SO_2, NO_2 and O_3 along with simulated winds in January 2014 in the NCP is shown in Fig. S2. The simulations of four air pollutants distributions are general in good agreement with the observations in the NCP, while partly biases of modeling still exist. It shows that the air in the NCP in January 2014 is much polluted with the monthly near-surface $PM_{2.5}$ concentrations over 150 μg m^{-3}. The observed and simulated highest average near-surface $PM_{2.5}$ concentrations are found in Beijing, Hebei, Henan, Shandong, north Anhui and north Jiangsu. Highest observed and simulated near-surface SO_2 and NO_2 concentrations almost occurs in same areas in the NCP. But simulated highest SO_2 concentrations are mainly concentrated around cities, while the distribution of NO_2 shows more area uniformly which likely due to their sources are different, the former mainly emits from point sources and the latter mainly comes from more area sources. The simulated O_3 concentrations are rather low in the NCP which is consistent with measurements.

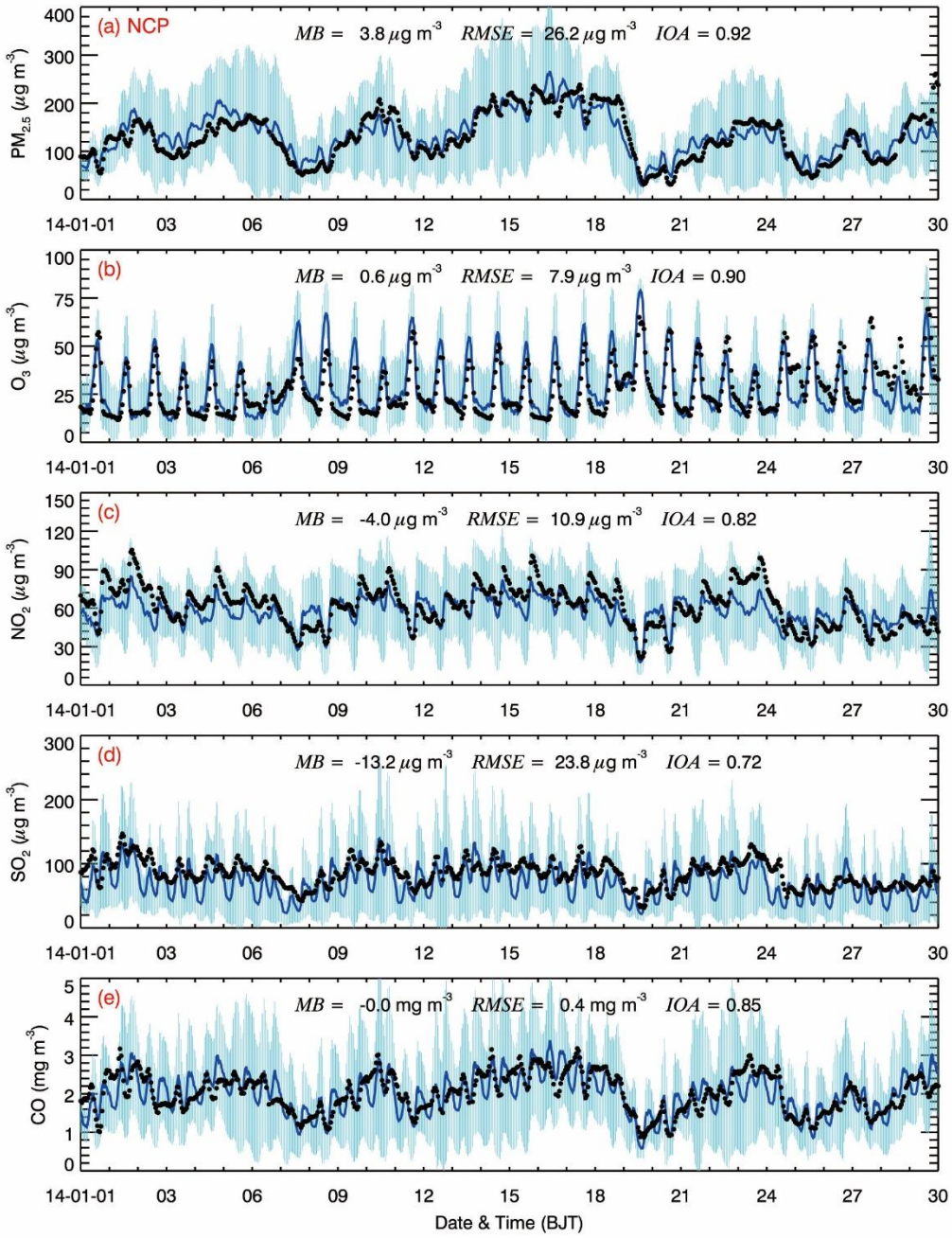

Figure S1. Comparison of observed (black dots) and simulated (dark blue lines) diurnal profiles of near-surface hourly mass concentrations of (a) $PM_{2.5}$, (b) O_3, (c) NO_2, (d) SO_2, and (d) CO averaged at monitoring sites in the NCP from January 1 to January 30, 2014. The light blue wavy lines represent error bars plotted using standard deviation.

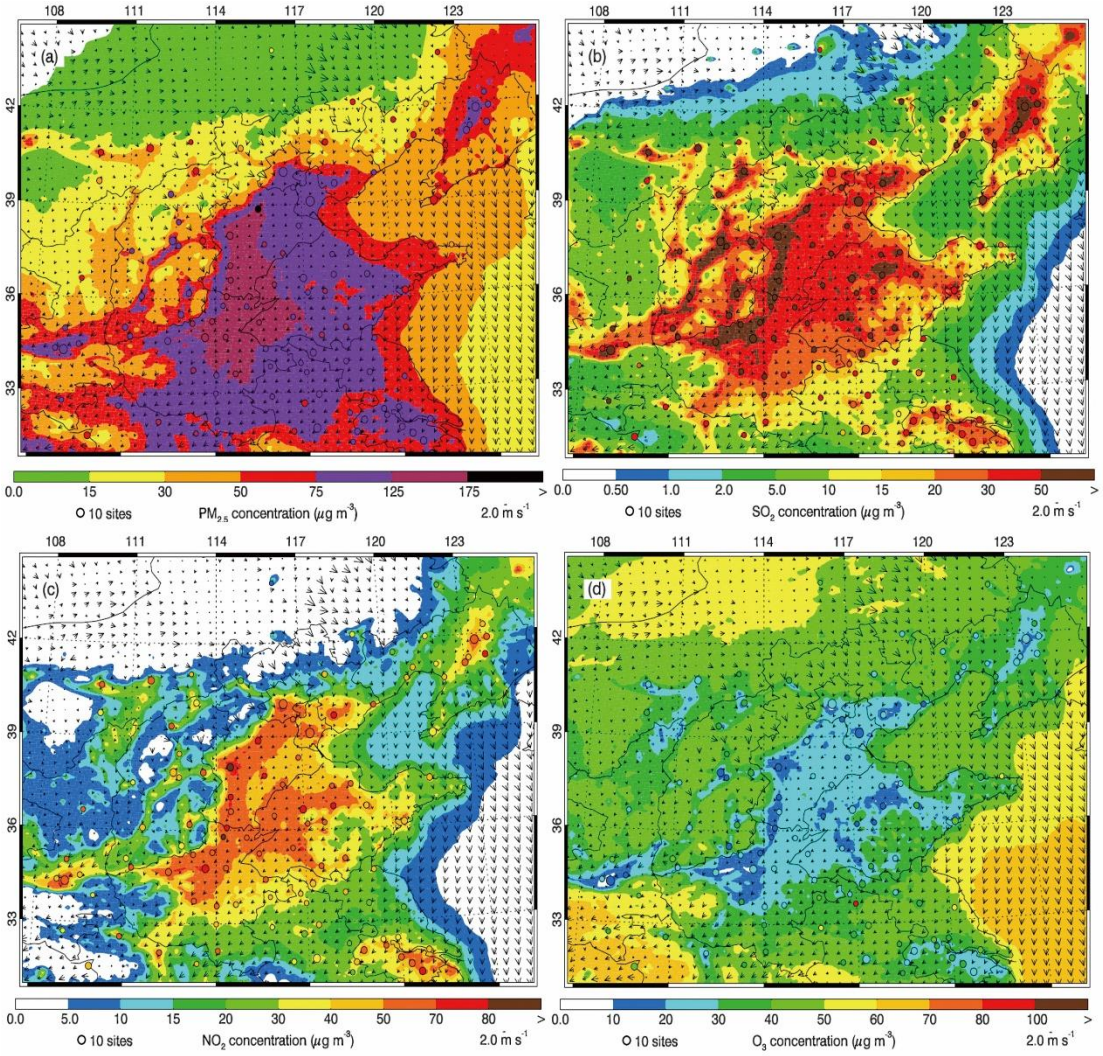

Figure S2. Pattern comparisons of simulated (color counters) vs. observed (colored circles) near-surface mass concentrations of (a) $PM_{2.5}$, (b) SO_2, (c) NO_2, and (d) O_3 averaged in January 2014. The black arrows indicate simulated surface winds.

Figure S3 provides the time series variations of simulated and observed aerosol species including OA (1.6 times of measurement OC), EC, ammonium, sulfate, and nitrate at Beijing and Tianjin city from January 1 to January 30, 2014. It shows that the WRF-Chem model generally predicts the temporal variations of the aerosol species against the field measurements reasonably with relatively high IOA value. The model yields the main peaks of aerosol species but with some frequently underestimates or overestimates which is mostly linked to the uncertainty of emission inventory and meteorological variations.

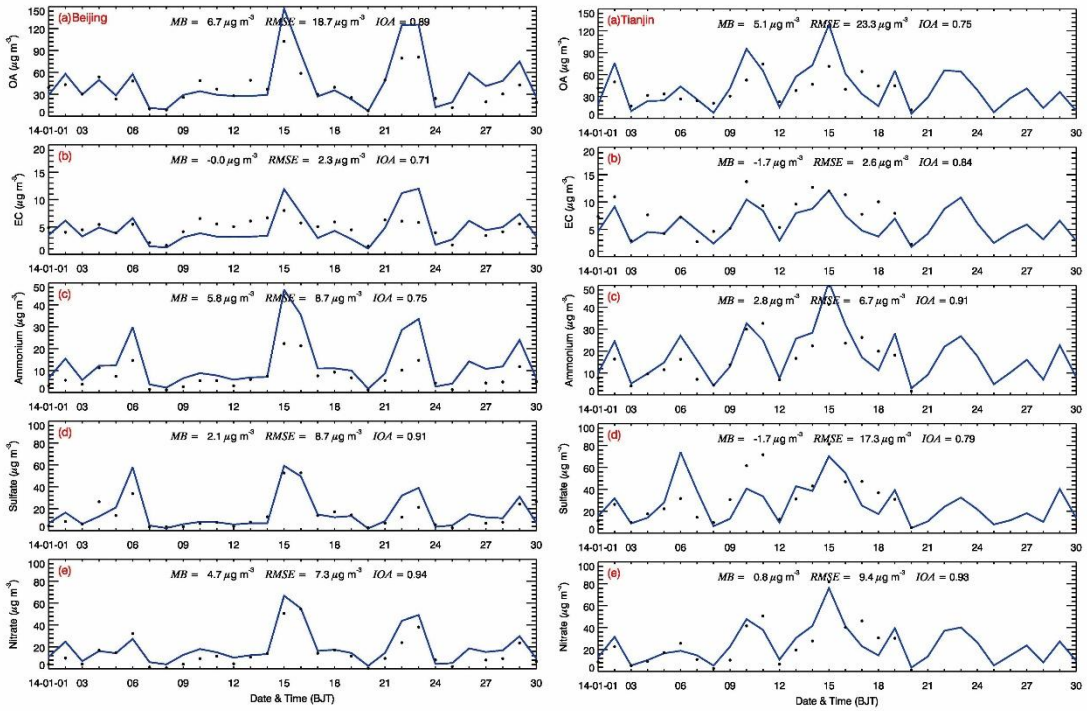

Figure S3. Comparison of measured (black dots) and simulated (blue lines) daily profiles of submicron aerosol species of (a) OA, (b) EC, (c) ammonium, (d) sulfate, and (e) nitrate at two sites (Beijing and Tianjin) in the NCP from January 1 to January 30, 2014.

S3.2 Downward shortwave flux comparison

Figure S4 shows the comparison of measured (black dots) and simulated (blue lines) diurnal profiles of the SWDOWN reaching the ground surface in (a) Beijing, (b) Tianjin, (c) Zhengzhou, (d) Hefei, and (e) Ji'nan from 01 January 2014 to 30 January 2014. Although the MB and RMSE values suggest bias in the model performance, but in overall, the model generally captures the diurnal patterns quite well, as reflected by the average IOA values up to 0.95 across all five cities. The biases of SWDOWN between model and field study may be caused by the cloud cover and optical thickness calculation in the model, which is due to the horizontal resolution of the model is insufficient to resolve the cumulus clouds.

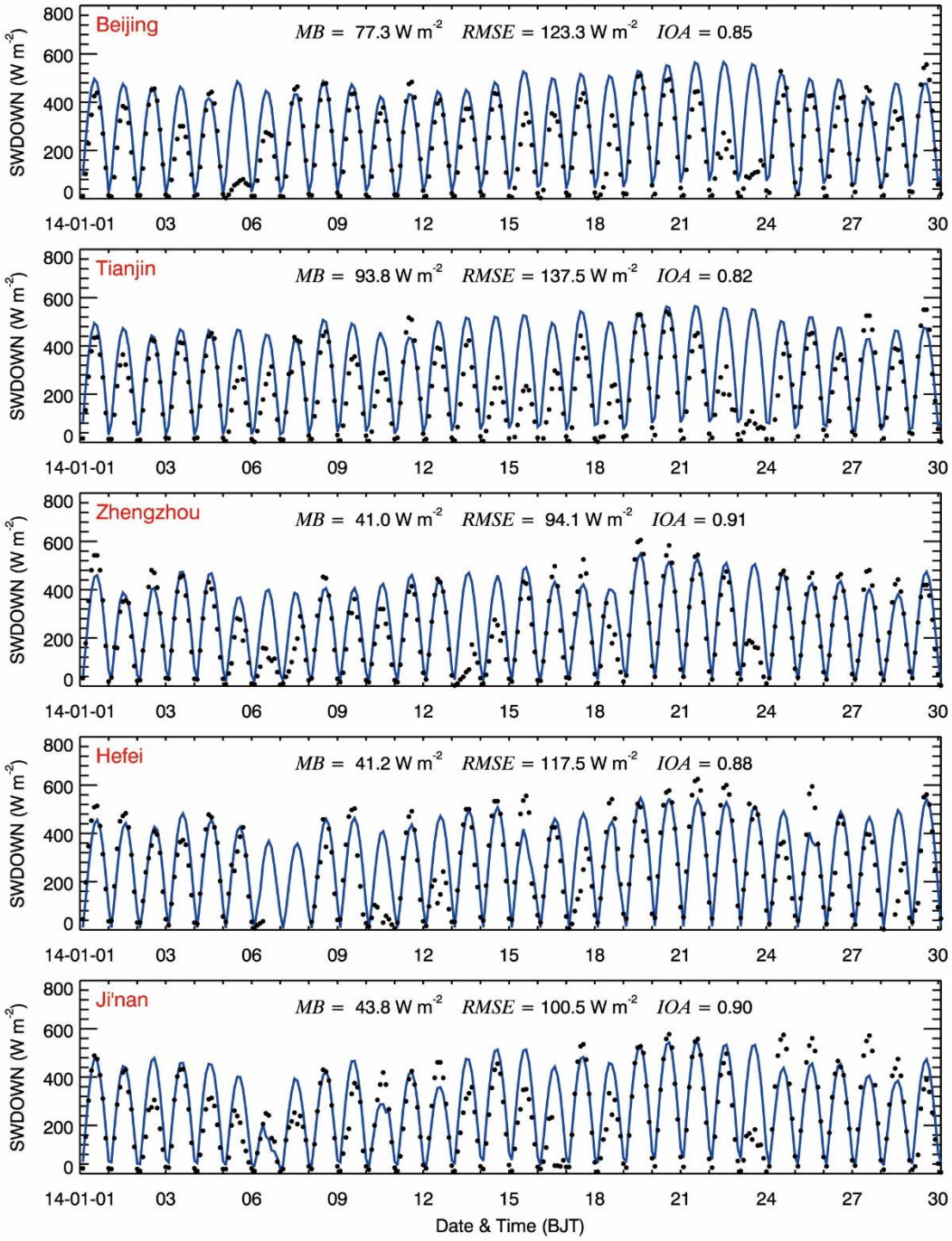

Figure S4. Comparison of measured (black dots) and simulated (blue lines) diurnal profiles of the SWDOWN reaching the ground surface in (a) Beijing, (b) Tianjin, (c) Zhengzhou, (d) Hefei, and (e) Ji'nan from January 1 to January 30, 2014.

S3.3 OA from different sources comparison in Beijing

Figure S5 presents a comparative analysis of temporal profiles of measured and simulated OA, POA from coal combustion (POA-COAL), biomass burning combustion (POA-BB), POA from vehicle exhaust (POA-TRA) and SOA in Beijing from January9 to 25, 2014. The model shows a good fit with

observed data with an IOA of 0.85, suggesting a reasonably accurate representation of OA variations, despite some discrepancies in peak values and slightly overestimates as indicated by an RMSE of 33.1 μg/m³ and an MB of 5.0 μg/m³, respectively. The model also generally tracks the measured diurnal variations in POA-COAL mass concentrations, with an IOA of 0.81. The model frequently underestimates or overestimates the POA-COAL mass concentrations and is also subject to missing the observed POA-COAL peaks. The POA-COAL is mainly emitted from industries and residential coal combustion. In general, the POA-COAL emissions from industries have clear diurnal variations but are opposite for those from residential coal combustion, causing large model biases for the POA-COAL simulation. The model performs well in capturing the general trend of POA-BB with an IOA of 0.86 and a lower RMSE of 4.0 μg/m³, while POA-Tra has a lower IOA of 0.56. Although the model captured the major vehicle pollution events, some smaller peaks were not well reflected in the model. Modeled SOA shows a fair correlation with observed data (IOA of 0.73) but also exhibits some of the higher variance in peak concentrations, reflected in an RMSE of 11.3 μg/m³. In general, the IOA values of all types of OA suggest a reasonable model performance, particularly in capturing the temporal dynamics with some quantitative in accuracies which largely associated with the influence of meteorological conditions and emission sources uncertainties.

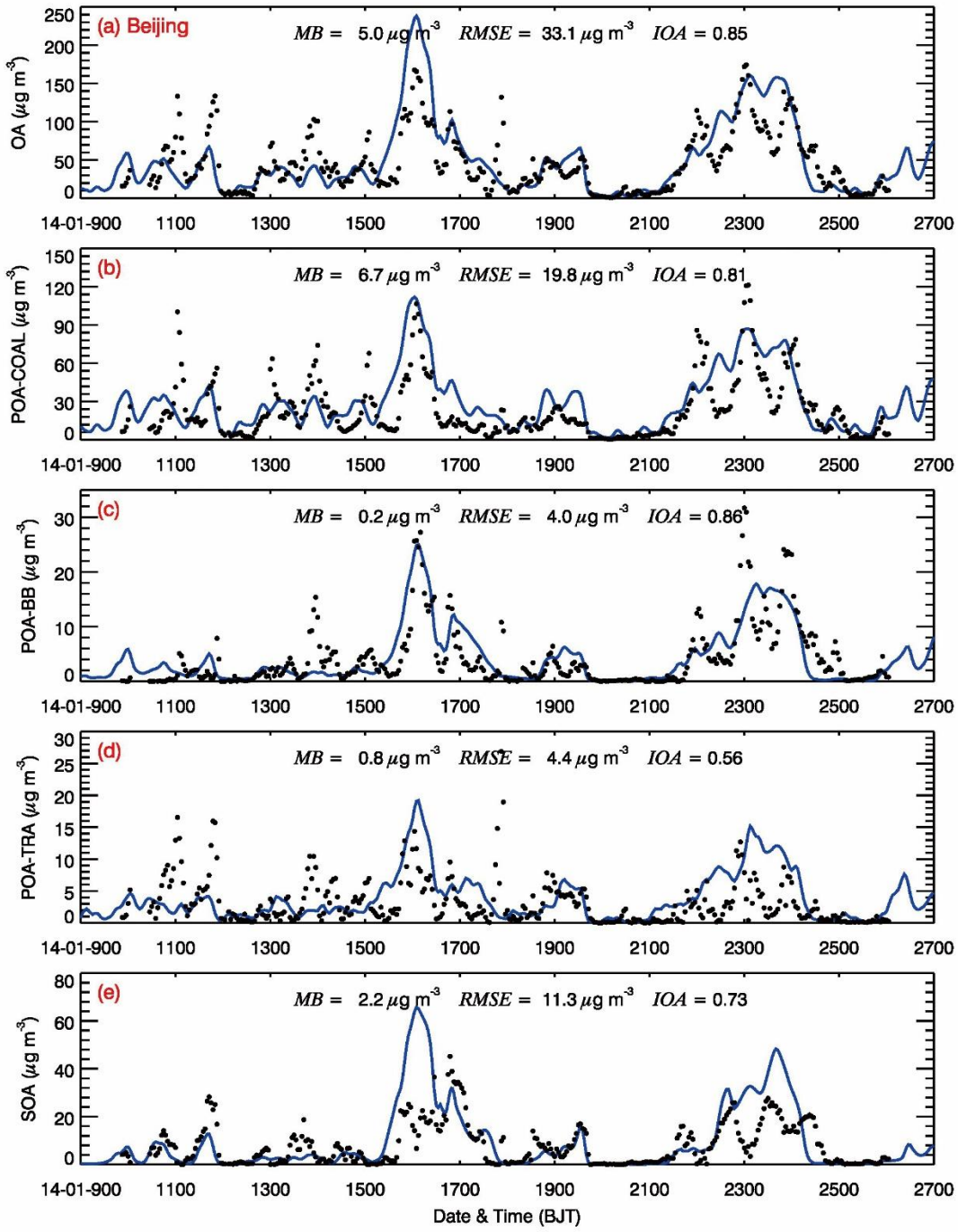

Figure S5. Temporal profiles of measured (black dots) and simulated (blue lines) OA (a), POA-Coal (b), POA-BB (c), POA-Tra (d) and SOA (e) in Beijing from January 9 to 25, 2014.

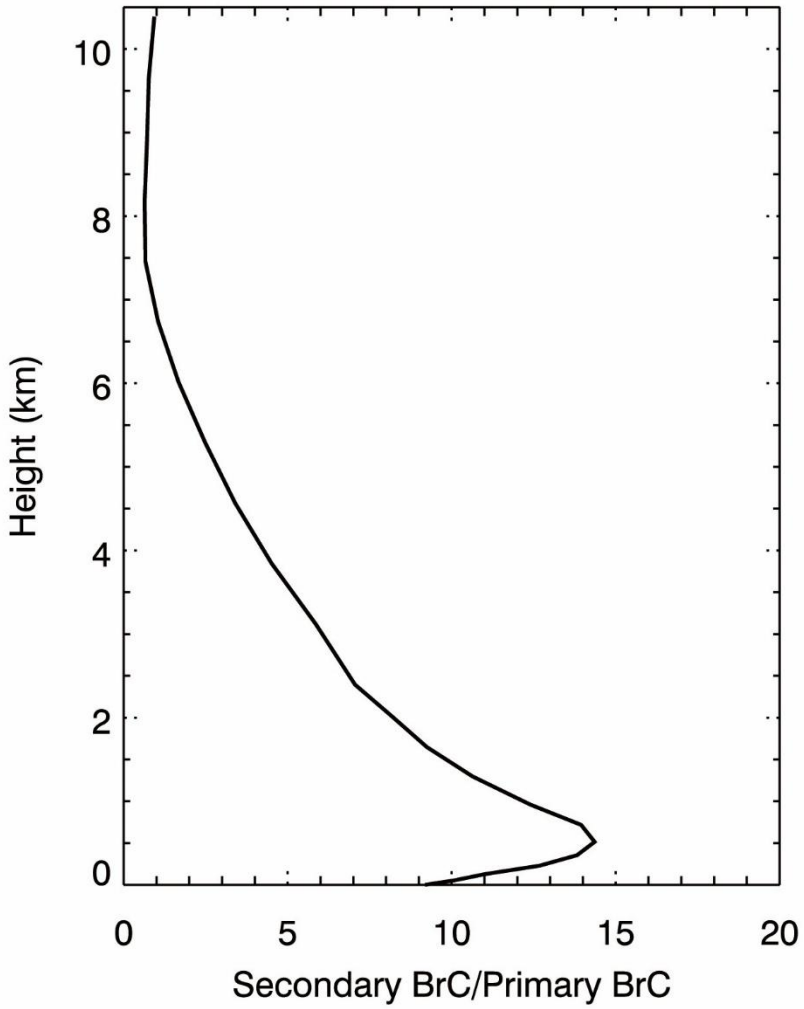

153

154 **Figure S6. Vertical profile of secondary BrC to primary BrC ratio in NCP in January, 2014**

155

References

Binkowski, F. S. and Roselle, S. J.: Models-3 Community Multiscale Air Quality (CMAQ) model aerosol component 1. Model description, J. Geophys. Res., 108, 479, https://doi.org/10.1029/2001JD001409, 2003.

Chen, F. and Dudhia, J.: Coupling an Advanced Land Surface–Hydrology Model with the Penn State–NCAR MM5 Modeling System. Part I: Model Implementation and Sensitivity, Mon. Wea. Rev., 129, 569–585, https://doi.org/10.1175/1520-0493(2001)129<0569:CAALSH>2.0.CO;2, 2001.

Chou, M. D. and Suarez, M. J.: A solar radiation parameterization for atmospheric studies, NASA Technique Report, Greenbelt, USA, NASA/TM-1999-104606/VOL15, 1999.

Chou, M. D., Suarez, M. J., Liang, X. Z., Yan, M. H., and Cote, C.: A Thermal Infrared Radiation Parameterization for Atmospheric Studies, NASA Technique Report, Greenbelt, USA, NASA/TM-2001-104606/VOL19, 2001.

Chow, J. C., Watson, J. G., Chen, L. W. A., Arnott, W. P., Moosmüller, H., and Fung, K.: Equivalence of elemental carbon by thermal/optical reflectance and transmittance with different temperature protocols, Environmental science & technology, 38, 4414–4422, https://doi.org/10.1021/es034936u, 2004.

Elser, M., Huang, R.-j., Wolf, R., Slowik, J. G., Wang, Q., Canonaco, F., Li, G., Bozzetti, C., Daellenbach, K. R., Huang, Y., Zhang, R., Li, Z., Cao, J., Baltensperger, U., El-Haddad, I., and Prévôt, A. S. H.: New insights into $PM_{2.5}$ chemical composition and sources in two major cities in China during extreme haze events using aerosol mass spectrometry, Atmos. Chem. Phys., 16, 3207–3225, https://doi.org/10.5194/acp-16-3207-2016, 2016.

Feng, T., Li, G., Cao, J., Bei, N., Shen, Z., Zhou, W., Liu, S., Zhang, T., Wang, Y., Huang, R.-j., Tie, X., and Molina, L. T.: Simulations of organic aerosol concentrations during springtime in the Guanzhong Basin, China, Atmos. Chem. Phys., 16, 10045–10061, https://doi.org/10.5194/acp-16-10045-2016, 2016.

Grell, G. A., Peckham, S. E., Schmitz, R., McKeen, S. A., Frost, G., Skamarock, W. C., and Eder, B.: Fully coupled “online” chemistry within the WRF model, Atmospheric Environment, 39, 6957–6975, https://doi.org/10.1016/j.atmosenv.2005.04.027, 2005.

Guenther, A., Karl, T., Harley, P., Wiedinmyer, C., Palmer, P. I., and Geron, C.: Estimates of global terrestrial isoprene emissions using MEGAN (Model of Emissions of Gases and Aerosols from Nature), Atmos. Chem. Phys., 6, 3181–3210, https://doi.org/10.5194/acp-6-3181-2006, 2006.

Hess, P. G., Flocke, S., Lamarque, J.-F., Barth, M. C., and Madronich, S.: Episodic modeling of the chemical structure of the troposphere as revealed during the spring MLOPEX 2 intensive, J. Geophys. Res., 105, 26809–26839, https://doi.org/10.1029/2000JD900253, 2000.

Hong, S. Y. and Lim, J.O.J.: The WRF single-moment 6-class microphysics scheme (WSM6), Asia Pacific Journal of Atmospheric Sciences, 42, 129–151, 2006.

Horowitz, L. W., Walters, S., Mauzerall, D. L., Emmons, L. K., Rasch, P. J., Granier, C., Tie, X., Lamarque, J.-F., Schultz, M. G., Tyndall, G. S., Orlando, J. J., and Brasseur, G. P.: A global simulation of tropospheric ozone and related tracers: Description and evaluation of MOZART, version 2, J. Geophys. Res., 108, n/a-n/a, https://doi.org/10.1029/2002JD002853, 2003.

Janjić, Z. I.: Nonsingular Implementation of the Mellor-Yamada Level 2.5 Scheme in the NCEP Meso Model, 437, Ncep Office Note, Camp Springs, USA, 2002.

Li, G., Lei, W., Bei, N., and Molina, L. T.: Contribution of garbage burning to chloride and $PM_{2.5}$ in Mexico City, Atmos. Chem. Phys., 12, 8751–8761, https://doi.org/10.5194/acp-12-8751-2012, 2012.

Li, G., Bei, N., Tie, X., and Molina, L. T.: Aerosol effects on the photochemistry in Mexico City during MCMA-2006/MILAGRO campaign, Atmos. Chem. Phys., 11, 5169–5182, https://doi.org/10.5194/acp-11-5169-2011, 2011a.

Li, G., Zavala, M., Lei, W., Tsimpidi, A. P., Karydis, V. A., Pandis, S. N., Canagaratna, M. R., and Molina, L. T.: Simulations of organic aerosol concentrations in Mexico City using the WRF-CHEM model during the MCMA-2006/MILAGRO campaign, Atmos. Chem. Phys., 11, 3789–3809, https://doi.org/10.5194/acp-11-3789-2011, 2011b.

Li, G., Lei, W., Zavala, M., Volkamer, R., Dusanter, S., Stevens, P., and Molina, L. T.: Impacts of HONO sources on the photochemistry in Mexico City during the MCMA-2006/MILAGO Campaign, Atmos. Chem. Phys., 10, 6551–6567, https://doi.org/10.5194/acp-10-6551-2010, 2010.

Li, G., Zhang, R., Fan, J., and Tie, X.: Impacts of black carbon aerosol on photolysis and ozone, J. Geophys. Res., 110, 1042, https://doi.org/10.1029/2005JD005898, 2005.

Li, M., Liu, H., Geng, G., Hong, C., Liu, F., Song, Y., Tong, D., Zheng, B., Cui, H., Man, H., Zhang, Q., and He, K.: Anthropogenic emission inventories in China: a review, National Science Review, 4, 834–866, https://doi.org/10.1093/nsr/nwx150, 2017.

Li, X., Wu, J., Elser, M., Feng, T., Cao, J., El-Haddad, I., Huang, R., Tie, X., Prévôt, A. S. H., and Li, G.: Contributions of residential coal combustion to the air quality in Beijing–Tianjin–Hebei (BTH), China: a case study, Atmos. Chem. Phys., 18, 10675–10691, https://doi.org/10.5194/acp-18-10675-2018, 2018.

Liggio, J.: Reactive uptake of glyoxal by particulate matter, J. Geophys. Res., 110, 881, https://doi.org/10.1029/2004jd005113, 2005.

Nenes, A., Pandis, S. N., and Pilinis Christodoulos: ISORROPIA: A New Thermodynamic Equilibrium Model for Multiphase Multicomponent Inorganic Aerosols, Aquatic Geochemistry, 4, 123–152, 1998.

Robinson, A. L., Donahue, N. M., Shrivastava, M. K., Weitkamp, E. A., Sage, A. M., Grieshop, A. P., Lane, T. E., Pierce, J. R., and Pandis, S. N.: Rethinking organic aerosols: semivolatile emissions and photochemical aging, Science (New York, N.Y.), 315, 1259–1262, https://doi.org/10.1126/science.1133061, 2007.

Shrivastava, M. K., Lane, T. E., Donahue, N. M., Pandis, S. N., and Robinson, A. L.: Effects of gas particle partitioning and aging of primary emissions on urban and regional organic aerosol concentrations, J. Geophys. Res., 113, 2701, https://doi.org/10.1029/2007jd009735, 2008.

Tie, X.: Effect of clouds on photolysis and oxidants in the troposphere, J. Geophys. Res., 108, 23,073, https://doi.org/10.1029/2003JD003659, 2003.

Volkamer, R., San Martini, F., Molina, L. T., Salcedo, D., Jimenez, J. L., and Molina, M. J.: A missing sink for gas-phase glyoxal in Mexico City: Formation of secondary organic aerosol, Geophys. Res. Lett., 34, 641, https://doi.org/10.1029/2007GL030752, 2007.

Wesely, M. L.: Parameterization of surface resistances to gaseous dry deposition in regional-scale

numerical models, Atmospheric Environment (1967), 23, 1293–1304, https://doi.org/10.1016/0004-6981(89)90153-4, 1989.

Xing, L., Wu, J., Elser, M., Tong, S., Liu, S., Li, X., Liu, L., Cao, J., Zhou, J., El-Haddad, I., Huang, R., Ge, M., Tie, X., Prévôt, A. S. H., and Li, G.: Wintertime secondary organic aerosol formation in Beijing–Tianjin–Hebei (BTH): Contributions of HONO sources and heterogeneous reactions, Atmos. Chem. Phys., 19, 2343–2359, https://doi.org/10.5194/acp-19-2343-2019, 2019.

Zhang, Q., Streets, D. G., Carmichael, G. R., He, K. B., Huo, H., Kannari, A., Klimont, Z., Park, I. S., Reddy, S., Fu, J. S., Chen, D., Duan, L., Lei, Y., Wang, L. T., and Yao, Z. L.: Asian emissions in 2006 for the NASA INTEX-B mission, Atmos. Chem. Phys., 9, 5131–5153, https://doi.org/10.5194/acp-9-5131-2009, 2009.

Zhang, T., Cao, J. J., Tie, X. X., Shen, Z. X., Liu, S. X., Ding, H., Han, Y. M., Wang, G. H., Ho, K. F., Qiang, J., and Li, W. T.: Water-soluble ions in atmospheric aerosols measured in Xi'an, China: Seasonal variations and sources, Atmospheric Research, 102, 110–119, https://doi.org/10.1016/j.atmosres.2011.06.014, 2011.

Zhao, J., Levitt, N. P., Zhang, R., and Chen, J.: Heterogeneous reactions of methylglyoxal in acidic media: Implications for secondary organic aerosol formation, Environmental science & technology, 40, 7682–7687, https://doi.org/10.1021/es060610k, 2006.